REVISITING EFFECTS OF NITROGEN INCORPORATION AND GRAPHITIZATION ON CONDUCTIVITY OF ULTRA-NANO-CRYSTALLINE DIAMOND FILMS

By

Tanvi Nikhar

A THESIS

Submitted to
Michigan State University
in partial fulfillment of the requirements
for the degree of

Electrical Engineering – Master of Science

2019

ABSTRACT

REVISITING EFFECTS OF NITROGEN INCORPORATION AND GRAPHITIZATION ON CONDUCTIVITY OF ULTRA-NANO-CRYSTALLINE DIAMOND FILMS

By

Tanvi Nikhar

Diamond has many superior electric and electronic properties over other materials, yet its application in electronic devices is severely limited due to difficulties in producing *n*-type conductivity in diamond as available dopants all have activation energy much larger than the thermal energy, kT, at room temperature. The substitutional doping of nitrogen in grain boundaries of granular graphitic-rich ultra-nanocrystalline diamond (UNCD) films provides for high conductivities even at room temperature with an apparent activation energy to be much lower than kT. Such low activation energy is a consequence of the formation of new electronic states associated with carbon and nitrogen near and above the Fermi level. However, the relative contribution of sp^2 graphitic phase and incorporated nitrogen to the conduction of the films remains unclear.

In the present work, structural and electrical properties of nitrogen-incorporated (N)UNCD films are studied as a function of deposition temperature and nitrogen concentration in the precursor synthesis gas mixture consisting of H_2, CH_4 and N_2. Four sets of (N)UNCD films with 0%, 5%, 10% and 20% nitrogen concentration in the synthesis gas were produced by microwave assisted chemical vapor deposition on intrinsic (100)-oriented Si substrates.

Resistance tunability over a range of about 4 orders of magnitude was achieved by varying the growth parameters. Raman spectroscopy and scanning electron microscopy (SEM) results show that the UNCD films undergo a progressive and highly reproducible material phase transformation, from ultra-nano-diamond to nanocrystalline graphite as deposition temperature increases. Addition of nitrogen increases the amount of sp^2 bonded carbon in the films thus enhancing the physical connectivity in the grain boundary network that have high electronic state density and leads to improved conductivity. However, crystallinity of sp^2 carbon phase remains another (previously underestimated) major factor in determining the conductivity of (N)UNCD films.

ACKNOWLEDGEMENTS

Firstly, I would like to express my sincere gratitude to my advisor, Dr. Baryshev, for his constant support and guidance throughout my Master's study, from encouraging me to work with my creative freedom to keeping me motivated during any setbacks.

This work would not have been possible without the resources made available to us at Fraunhofer USA Center for Coatings and Diamond Technologies and the technical expertise of Mr. Robert Rechenberg and other people at the facility.

I would also like to thank Dr. Hogan and Dr. Grotjohn for their encouragement and insights towards improving this work and willingly addressing any and everything that was needed during the process.

Finally, a special gratitude to my friends and family for keeping me sane in my moments of jitters and for their constant help and support throughout the duration of this project.

TABLE OF CONTENTS

LIST OF TABLES

LIST OF FIGURES

CHAPTER 1

INTRODUCTION

Diamond exhibits a unique combination of superior material properties including extreme hardness, high thermal conductivity, low coefficient of friction, high degree of chemical inertness [3]; that make it suitable for a diverse range of applications [4, 5, 6]. The potential of diamond to be used as electron emitter or amplifier, high flux particle and UV or X-ray detector, electrodes for electrochemistry and in active electronic devices has attracted the interest of the research and technology-oriented communities. More specifically, it is the low, and sometimes negative, electron affinity that makes diamond a good electron source. The high breakdown field in comparison with both silicon and gallium arsenide, large band gap, large thermal conductivity and large momentum relaxation time indicate a potential for diamond in high-frequency, high-temperature, high-power applications [7, 8].

Many proof-of principle two-terminal and three-terminal devices have been made and tested [9, 10, 11, 12]. However, the development of diamond devices poses great challenges due to problem with a large carrier activation energy of available dopants which necessitates specialized concepts (e.g. surface transfer doping) to allow room temperature operation [13, 14, 15]. *p*-type doping can be achieved with addition of boron, yielding an activation energy of 0.37 eV [16]. Along with hydrogen-induced surface conductivity (surface transfer doping), high performance devices have been reported with extremely low activation energy [17]. However, to date, problems with *n*-type doping of diamond [18, 19], in part due to its high atomic density, have hindered its development as a ubiquitous device material. Using nitrogen as a dopant is difficult as doping of bulk diamond with nitrogen produces a deep donor level of 1.7 eV below the conduction band. Other *n*-type dopants have been attempted, such as sulfur and phosphorus, with only limited success as the room-temperature conductivities are too low for the application of these materials in conventional electronic device architectures. A shallow donor species is still sought for diamond.

Another relevant issue related to the development of diamond film-based electronics, is that

currently single crystal diamond (SCD) films have been used to produce high power diamond-based electronic devices with promising performance [20, 21, 8]. However, SCD films can be grown only on SCD diamond and other relatively expensive substrates with very small areas, that is available for large scale integration. On the other hand, polycrystalline diamond (PCD) films have been demonstrated to grow on large areas and relatively inexpensive substrates with high uniformity [3], which with proper optimization have the potential to provide the base for the development of transformational diamond-based electronics.

Ultra-nanocrystalline diamond (UNCD) is another form of diamond which is shown to exhibit outstanding and tunable *n*-type conductivity, and excellent biocompatibility [22, 23, 24, 25], thus enabling a broad range of applications to a new generation of electronic devices including bio-medical devices. The unconventional properties of UNCD films are due to its microstructure characterized by randomly oriented nanosized diamond crystallites bonded together by grain boundaries [26, 27]. The complex bonding structure at these grain boundaries [28, 29] imparts a striking set of attributes to UNCD films, *viz*. dramatic difference in electron and phonon properties of UNCD (resulting in dramatic electrical and thermal conductivities) exists as compared to intrinsic SCD. The key difference is that new electronic state bands are introduced into the 5.5 eV band gap of bulk diamond due to dangling bonds and π-bonded carbon atoms present in the grain boundaries [29], which is further enhanced by the preferential incorporation of nitrogen in the GBs [30]. The incorporation of nitrogen via the addition of N_2 gas to the feed gas mixture brings about changes in morphology [31] and electronic structure within the grain boundaries that leads to orders of magnitude of change to the electrical conductivity [32]. The discussion on the exact mechanisms of the effects of N_2 on electronic properties of UNCD remains open.

1.1 Literature Review

The growth of nanocrystalline diamond by CVD process under hydrogen-poor and argon/carbon-rich conditions was first reported by Gruen et al. in 1994 [33, 34, 35]. The control of diamond microstructure through the crystallite size was further analyzed in 1999 [27] by replacing hydrogen

with argon in the growth process. Conventional diamond film CVD typically uses a gas mixture of 1% CH_4 in 99% H_2 where the incorporation of carbon in the diamond lattice is made possible through a series of hydrogen abstraction reactions on CH_4. Replacement of hydrogen with argon was done by using fullerene C_{60} as a precursor molecule which can dissociate in argon plasma to give carbon dimer C_2 from which diamond can nucleate and grow in the absence of hydrogen.

As argon replaces hydrogen in the initially 1% CH_4/H_2 balanced plasma (eventually yielding 1% CH_4/Ar balanced plasma), the morphology of the film transitions from well faceted microcrystalline diamond (MCD) with grain sizes of 0.5-2 μm and columnar growth structure to nanocrystalline diamond (NCD) with no observable morphological growth features due to the nano-scale size of the crystals. These NCD films were found to be composed of two components: nanodiamond crystallites (>95 vol.%) and amorphous carbon grain boundaries (<5 vol.%), made of either glassy carbon or tetrahedrally-bonded diamond-like amorphous carbon. The label ultra-nanocrystalline diamond (UNCD) was used to define a class of NCD having phase-pure diamond crystallites of size of 3-5 nm and 0.3 to 0.5 nm wide GB. The GBs retain ~10 vol.% of all the carbon atoms of the film having mixed sp^2 and sp^3 hybridization and unpaired electrons forming dangling bonds [36].

The synthesis and characterization of nitrogen-doped UNCD films (N-UNCD) was first reported by Bhattacharyya *et al*. in 2001 [32]. They examined the effect of changes in plasma chemistry on the film morphology and electrical transport properties as nitrogen was incorporated into the films. The films were grown in CH_4(1%)/Ar/N_2 plasma varying N_2 from 1% to 20% with all other parameters fixed. Dramatic increase in room-temperature conductivity was observed, increasing from 0.016 $\Omega^{-1}cm^{-1}$ (for 1% N_2) to 143 $\Omega^{-1}cm^{-1}$ (for 20% N_2), which represents an increase by roughly five orders of magnitude over undoped UNCD films. The latter value of conductivity was much higher than any other previously reported for n-type diamond and was comparable to heavily boron-doped p-type diamond [32]. Hall and Seebeck effect measurements confirmed the *n*-type nature of the conductivity for the nitrogen containing samples, as well as high and nearly temperature-independent values for the Hall mobility, with room temperature values in the range of 1 to 10 $cm^2V^{-1}s^{-1}$ in the case of highly conductive samples. All the reports that followed, confirmed

that addition of nitrogen to plasma yields greatly enhanced conductivity (N)UNCD; grown either by RF or HF CVD [37, 38].

Even so, how much nitrogen is required to bring the conductivity to the champion metrics of ~100 S/cm is still under debate. The same Argonne group reported that N_2 plasma content can lie within a very large range, between 8 to 20 %; as the conductivity increases as nitrogen is increased from 0 to 8% and saturates thereafter for all the higher nitrogen concentrations in the plasma upto 20% [37]. The main reason brought up to explain this effect was saturating nitrogen incorporation. Secondary ion mass spectroscopy (SIMS) showed a continuous increase in the incorporated nitrogen in the film as nitrogen was increased in the plasma with a maximum of 2.2×10^{20} cm^{-3} for 18% N_2 in the plasma [39]. This is in contradiction with other reports where the incorporated nitrogen was shown to initially increase but then saturate at $\sim2\times10^{20}$ atoms cm^{-3} for somewhere between 5-10% N_2 in the plasma which might also be a cause of the observed saturation in conductivity [32, 37].

Where does nitrogen go in the film? Originally, based on the tight binding molecular dynamics simulation results, it was determined that nitrogen is much more favored to be incorporated into the grain boundaries rather than grains. Indeed, high-resolution transmission electron microscopy (HRTEM) found that as the nitrogen content in the plasma is changed from 0% to 20%, the grain-boundary width increases from about 0.5 to 2.2 nm. Simultaneous grain growth from 4 to 16 nm was explained by the presence of CN at enhanced nitrogen content that does not itself lead to diamond growth but rather reduces the renucleation rate that results from C_2 dimer based diamond growth [31]. HRTEM also demonstrated that the GBs, being less dense than the grains, are built of sp^2 hybridized carbon [32].

Adding to that, electron energy-loss spectroscopy (EELS) spectra for the grains show phase pure diamond grains with sp^3 bonded carbon which does not change as nitrogen is added to the plasma. The grain boundary spectra indicate that the amount of sp^2 bonding increases only slightly while the sp^3 peak remains unchanged with nitrogen addition, keeping the ratio of sp^2 to sp^3 bonded carbon relatively unchanged. It is therefore concluded that the increase in sp^2 content in the film as a whole is derived from a slight increase in the grain-boundary material in the film, and not a

change in the local bonding structure within the grains or grain boundaries [31].

Near edge x-ray absorption fine structure (NEXAFS) results show that all films, even those deposited using high amounts of nitrogen in the growth plasma, have only a small fraction of sp^2-bonded carbon in the film, being remarkably similar to phase pure diamond and that as nitrogen is added to the film, the sp^2 bonding increases only slightly. The fraction of sp^2 to sp^3-bonded carbon is shown to increase from about 6.7% in undoped UNCD to 13.5% in 20% N_2 UNCD. This increase is proposed to be due to a larger total volume of grain boundaries with the same sp^2/sp^3 ratio based on previous HRTEM results [39].

Theoretical models predict that UNCD grain boundary defects produce a number of states in the forbidden band of diamond: π and π^* states for the sp^2-bonded atoms and σ^* states for the sp^3-coordinated atoms forming a continuous band of delocalized energy states, across which conduction takes place. When nitrogen is incorporated at the grain boundaries, new electronic states are further introduced into the band gap. At the same time, a strong morphology change resulting from more than 10% addition of nitrogen to the plasma could lead to an increase in the robustly physically connected grain boundaries aiding conductivity.

There is therefore a contradiction whether nitrogen doping takes place or whether nitrogen mediates enhanced conductivity by promoting grain growth (and their connectivity). The contradiction is further introduced by the results of Ikeda *et al*. who found the strong dependence of conductivity on the deposition temperature (T_d) which was due to the changes induced in the structure of nanodiamond while addition of nitrogen did not play much role [40]. More specifically, the room temperature resistivity decreases exponentially by more than three orders of magnitude when T_d rises to 1200 K, and then saturates at $\sim 10^{-2}$ Ωcm for further increase in T_d. The structure of GB which is mainly composed of amorphous sp^2-bonded carbon is expected to vary significantly with T_d because T_d promotes a transformation from sp^3- to sp^2-bonded carbon, thus increasing conduction.

Room temperature resistivity recorded for films grown at T_d=1100 and 1200 K as a function of gas-phase N_2 concentration show that for both T_d, the resistivity decreases by two to three

orders of magnitude upon 3%N_2 addition and saturates for further N_2 up to 30% [40]. This is in accordance with previously observed saturation in conductivity for higher nitrogen content in the plasma [37]. The minimum resistivity in the saturation region is lower for higher T_d film. Since the incorporated nitrogen concentration measured by XPS is constant at about 0.3 at. % at all gas phase N_2 concentrations and also for both T_d (saturation effect seen before [32, 37]), it is concluded that sp^2 phase (dependent upon T_d in this case) is more responsible for increasing conduction than the nitrogen concentration itself. It also agrees with previous observations in that, it is not as much the incorporated nitrogen as is the relative increase in the sp^2 content induced by nitrogen that ultimately affects conductivity.

The T_d studies done by Ikeda *et al*. though, for different N_2 concentrations is only limited to two T_d values with no analysis of the structure and various phases present in the film and how their change is related to conductivity. Exceptional conductivity tunability down to 100 S/cm based on only varying T_d was recently further discussed in detail by J.J. Alcantar-Pena *et al*.. [41] for undoped (no N_2 in plasma) UNCD.

The same study emphasized the critical importance of Raman spectroscopy in studying UNCD even though it had been a premier method in characterizing diamond. The Raman of (N)UNCD features two major optical bands called D and G. Monitoring I(D)/I(G) ratio as well as the D and G band peak positions reveal particularly that the material is highly "dynamic", i.e it undergoes many simultaneous modifications as nitrogen and/or sp^2 phase is injected via adjusting plasma N_2 content or substrate temperature during growth. The D and G bands not only monitor diamond-to-graphite ratio but also trace down structural disorder. For example, a clear shift of the G band peak towards a higher wavenumber for higher T_d, which has never been addressed in literature. The general serious problem exists as there is vast variation of Raman spectra all interpreted as UNCD form of diamond, thus raising a challenging question as to what UNCD is and what is the range of application of this term as the Raman spectrum modifies from nearly NCD to nearly graphite type of fingerprint spectra. UNCD definition further fades away as UNCD was introduced to only grow in Ar rich or balanced plasmas [33, 34, 35, 42] while UNCD was shown to grow in H_2 balanced

plasmas as well [43].

To conclude, there is no consistent and complete understanding of the factors responsible for conduction in (N)UNCD films. Following details about these factors are still not clear: *i*) the phase of the sp^2 carbon and *ii*) the changes in energy space, physical space or both due to N_2 incorporation. Electron transport can be explained based on two competitive processes. First, an increase in the spatial connectivity of sp^2-bonded carbon is expected from the rise in the relative amount of sp^2-bonded carbon. This causes a better overlap of the electron orbitals among the sp^2 clusters and enhances the delocalization of the π and π^* states making electron transport more probable and increasing the electron mobility. Second, the decrease in the relative amount of diamond, increases the mean distance between diamond grains forming a spatially heterogeneous band structure. The system then behaves as grains and grain boundaries embedded in amorphous matrix. The relative contribution of these factors is also not clear. From the literature overview in the past 18 years, the community has moved from nitrogen doping [32] to geometrical and graphitization effects [43, 41]. The issue can be reduced to a very simple question – is it a conventional doping or just size effect, or both, that promotes high conductivity?

1.2 Thesis Objectives

1) The clear feasibility of engineering grain boundary structure to obtain tailored resistivity of UNCD films paves a way to the development of diamond based electronic power and bio-medical devices. Resistivity tunability has been studied either through the variation of plasma nitrogen concentration or deposition temperature, but never both. Both of these two synthesis variations have been shown to alter the physical and electronic density of state structure of UNCD being intertwined. The objective of this work is therefore to systematically vary both N_2 content and deposition temperature to better assess the physical mechanisms transforming UNCD from high to low resistive state.

2) The definition of UNCD based on Raman spectra is still vague as there is no definite set of features that can be conclusively identified as representative of UNCD. In addition to this, these

features are not analyzed in detail to completely interpret the changes in the position, shape and intensity of the peaks with changing growth conditions. For instance, the significant shift in the G band for both varying crystallite sizes and for varying N_2 concentration in the plasma as seen in the visible Raman spectra is either not addressed at all [44, 40, 42] or not understood [39]. Another objective of this work is to revisit interpretation of Raman spectra that contain information of all carbon phases present in UNCD and their crystallinity to shed light onto conductivity in UNCD and the basic definition of the term UNCD.

CHAPTER 2

CHEMICAL VAPOR DEPOSITION

Synthesis of diamond [1] using high-temperature, high pressure processes, in which diamond is the stable form of carbon, as can be seen in Fig. 2.1, has proved to be commercially successful but is not amenable to direct deposition of diamond on substrates or to large-area deposition. A distinctive method of diamond synthesis at low pressures, in which diamond is metastable with respect to graphite has offered the capability of direct deposition of diamond on a variety of substrates and has opened the possibility of new applications of diamond. In low-pressure diamond synthesis, common sources of carbon, eg. methane, are transformed by chemical vapor deposition (CVD) to diamond at atmospheric or sub atmospheric pressures and at temperatures that are common to materials processing.

Formation of diamond from nascent carbon containing species under metastable conditions is both thermodynamically allowed and readily achieved under proper deposition conditions which can be achieved by a variety of methods. These methods share certain generic features which include:

(i) **Gaseous Feedstock**- The gaseous feedstock includes at least one source of carbon-containing species, like methane; and a diluting gas such as hydrogen, as used by most methods. The energy provided to the system breaks down the carbon-containing gas into a variety of subspecies which are involved in donating a carbon atom to the growing diamond film on the substrate. It also breaks down the hydrogen gas, producing large amounts of atomic hydrogen which play which assist the growth process.

(ii) **Energy Source**- A means to provide energy to the deposition chamber is required to break down the input gases. Various CVD methods have been developed based on the source of energy such as thermally assisted hot-filament and plasma torch deposition, combustion

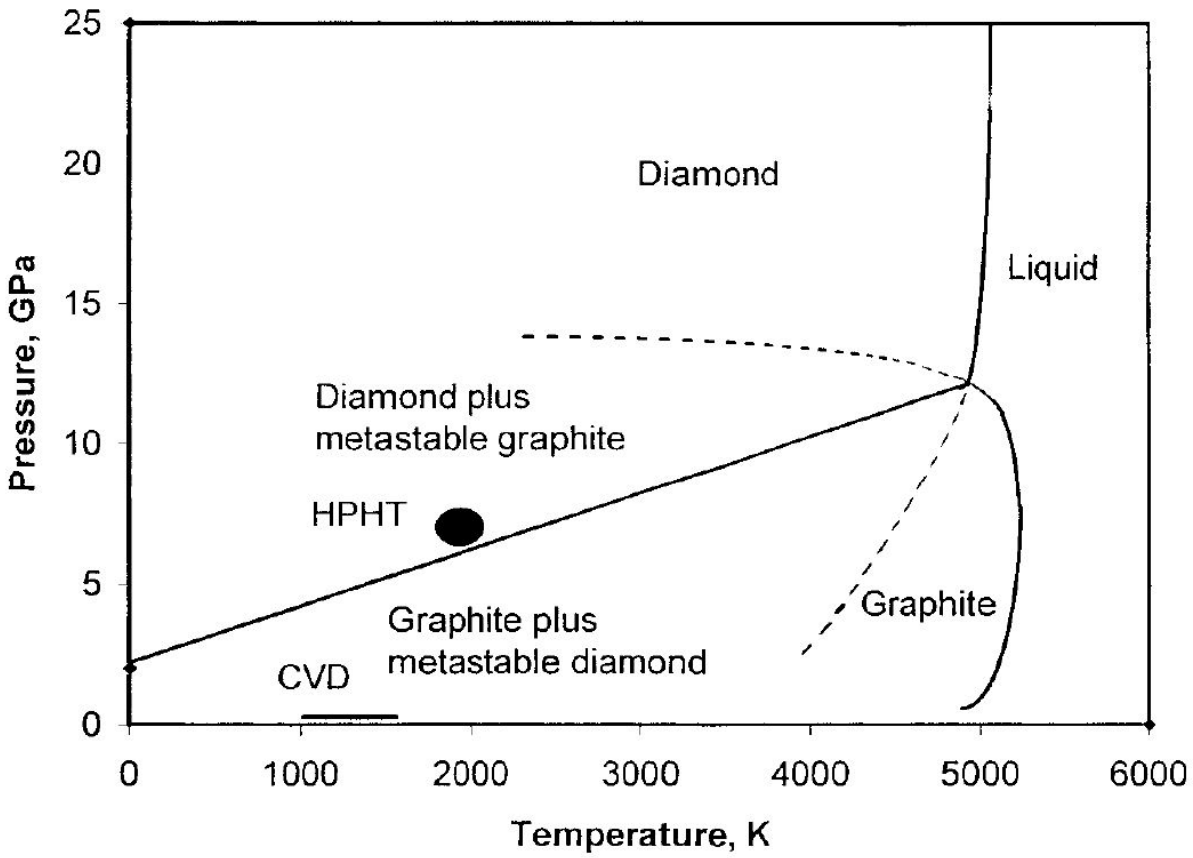

Figure 2.1: Phase diagram of carbon. Regions of metastability of diamond and graphite are bounded by extensions of the melting curves of diamond and graphite, respectively as shown by dashed lines. Approximate regions for high-pressure, high-temperature (HPHT) and chemical vapor deposition (CVD) synthesis of diamond are shown [1].

synthesis, laser-assisted and optically pumped techniques, and dc arc jet, rf and microwave plasma-assisted deposition based on electrical energy inputs.

(iii) **Substrate on which the film grows**.

2.1 Heteroepitaxial Film Growth

Diamond films can be grown on non-diamond substrates using CVD processes by treating or seeding the substrate to initiate and enhance the nucleation of diamond. There are several substrate surface pre-treatment methods like polishing with diamond powder, ultrasonic treatment in a slurry of micro or nano-sized diamond powder, bias enhanced nucleation, pulsed-laser irradiation, carburization,

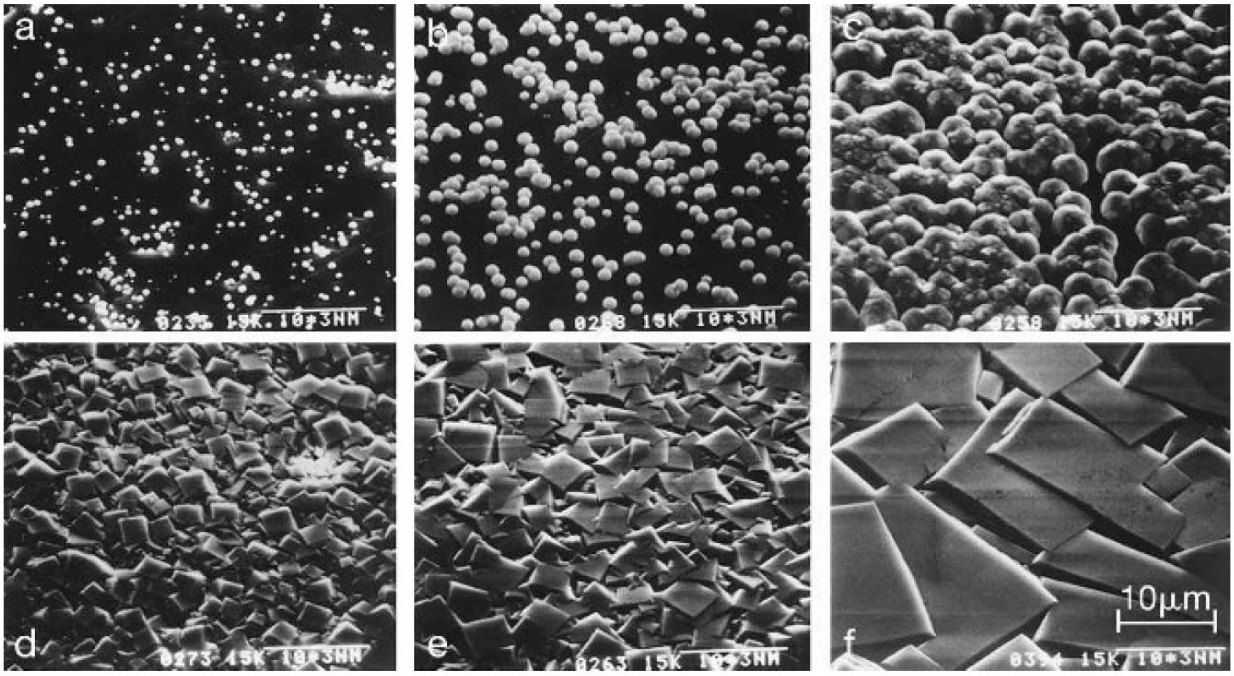

Figure 2.2: Diamond growth on a nondiamond substrate in sequential steps shown through SEM images: (a) nucleation; (b and c) growth of individual crystallites; (d) faceting and coalescence of crystallites; (e and f) continuous film growth [2].

chemical etching, coating with carbon materials. These seeds/defects introduced on the substrate, when exposed to the diamond growth environment, convert to nuclei of crystalline diamond or serve as nucleation sites via a heterogeneous nucleation mechanism. High surface nucleation density leads to better diamond-substrate adhesion, improves the homogeneity of the film and reduces the formation of voids at the substrate interface, thus reducing surface roughness.

Conventional growth of polycrystalline diamond generally consists of up to five distinguishable stages [1]: (1) The system undergoes an incubation period followed by (2) three-dimensional nucleation of individual crystallites on the substrate surface which ceases when all the activated nucleation active sites have been occupied or when the discrete crystallites grow together and completely cover the surface. (3) Subsequently, the individual crystallites grow three-dimensionally and develop faceting due to the relatively high rate of surface carbon diffusion from the surrounding substrate surface. (4) Once the crystals grow large enough to impinge upon one another, they coalesce, forming grain boundaries and then (5) continue growing homoepitaxially as a continuous

film, exhibiting competitive crystal growth. These different stages are illustrated by the micrographs shown in Fig. 2.2.

Often some degree of non-diamond carbon is incorporated during this nucleation and coalescence stage. The growth chemistry (gaseous carbon species, atomic hydrogen, dopant/impurity concentration etc.) and substrate temperature determine the morphology, quality, doping and degree of bulk defects in the film.

2.2 Growth Chemistry

The initiation of the gaseous chemistry is dominated by the dissociation of 1-40 % of the molecular hydrogen into atomic hydrogen. The subsequent gaseous chemistry is driven by reactions of atomic hydrogen with hydrocarbon species and reactions among the hydrocarbon species. With a hydrocarbon precursor such as CH_4, gas-phase hydrogen abstraction reactions lead to the generation of the methyl radical $CH_3^{\cdot}$, which adsorbs on a carbon radical site also created by hydrogen abstraction from the hydrogen-terminated growing diamond surface.

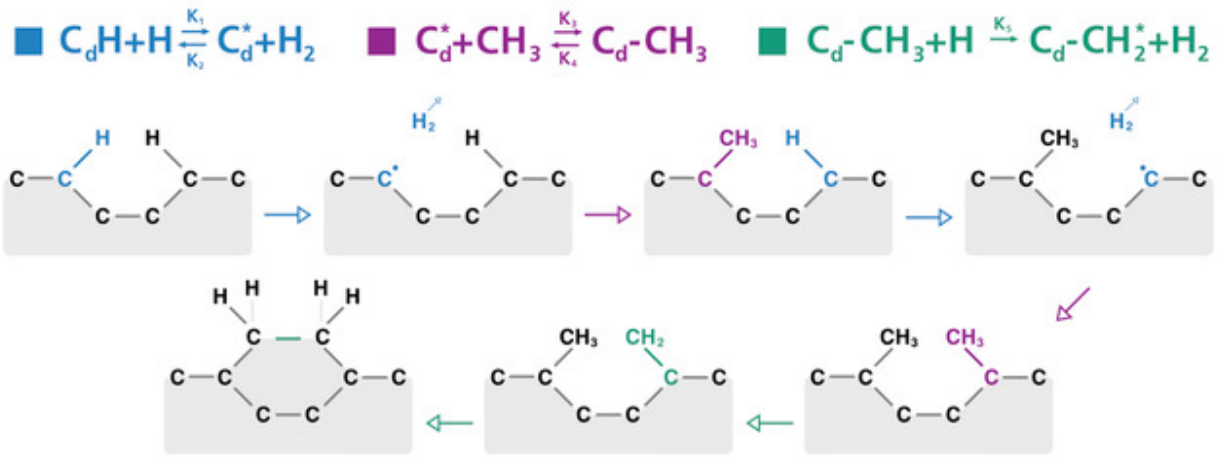

Figure 2.3: Hydrogen abstraction reactions leading to the incorporation of carbon in the diamond lattice during the growth process of poly crystalline diamond. (Courtesy: Fraunhofer CCD)

Additional hydrogen abstraction reactions (shown in Fig. 2.3) allow the carbon in the absorbed methyl radical to form carbon-carbon bonds and thus be incorporated into the diamond lattice

[27, 45]. Because graphite is thermodynamically more stable than diamond in the given growth environment, the growth of metastable diamond is stabilized by the presence of atomic hydrogen which removes graphitic nuclei when they do form because of the preferential etching of graphite over diamond.

2.3 Microwave Plasma CVD System

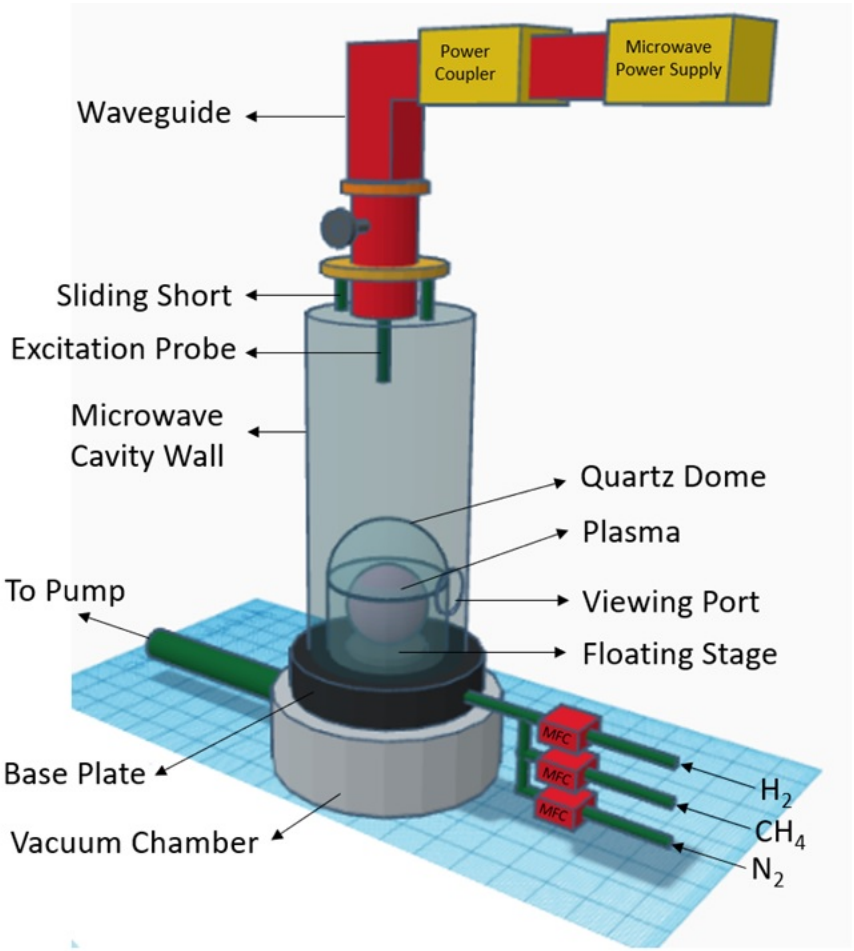

Figure 2.4: Schematic of the MPCVD system used for the growth of UNCD films in present work.

The role of the microwave plasma-assisted machine in the deposition of diamond is to create the chemical/thermal environment needed for diamond deposition. The microwave plasma-assisted diamond CVD (MPCVD) system used for the growth of UNCD films in this work is shown in

Fig. 2.4. It consists of various subsystems, that work in unison, under computer control, to provide the required deposition environment.

A magnetron power supply generates the microwave power which is supplied to the discharge chamber via the microwave energy coupling system consisting of a waveguide, cavity resonator and antenna to guide the microwave energy required to create and maintain the plasma discharge. The tuning elements for impedance matching of the waveguide to the reactor load influence the plasma discharge shape and size, directly impacting the uniformity of diamond deposition across the deposition surface.

The discharge chamber confines the plasma discharge and positions the substrate surface for optimum deposition. The substrate is placed on a stage which can be used in actively cooled or floating configuration to control the substrate temperature. A microwave transparent dome couples the microwave power while providing a gastight chamber. The flow rate of the feed gases to be delivered to the discharge chamber is controlled via mass flow controllers (MFC). The pressure control system pumps the reacted gas from the deposition chamber in a continuous manner and maintains the desired pressure using an adjustable (throttle) valve located between the pump and the deposition chamber.

CHAPTER 3

UNCD GROWTH AND ANALYSIS

3.1 Sample Growth

3.1.1 Deposition Chamber

Ultra-nanocrystalline diamond films were grown using MPCVD technique in a microwave cavity plasma reactor (MCPR) developed at Michigan State University and Wavemat/Norton in 1986-1995 [1]. The microwave discharge is produced inside a quartz dome which is located at one end of a microwave cavity. The cavity is formed by a cylindrical wall and a movable top short defining the top end of the cavity. The microwave energy is transmitted from a 2.45-GHz microwave generator through a rectangular waveguide to a transition into a coaxial waveguide that ends as a length adjustable excitation probe in the cylindrical cavity.

A hemispherical plasma discharge is created and is placed in direct contact of the substrate by adjusting the length of the probe and the location of the sliding short (L_s). The diameter of the microwave cavity is 17.8 cm with the substrate holder being able to accommodate substrate sizes up to 7.6 cm in diameter. The sliding short height L_s is adjusted to a length of approximately 21 cm. This cavity height produces a TM_{013} resonant microwave mode.

3.1.2 Substrate Preparation

The substrates used for growth were intrinsic (100)-oriented Si wafers of 0.6mm thickness and approximately 10×10 mm^2 cross-section having sheet resistance of 5MΩ/□. These substrates were ultrasonically cleaned in acetone to remove oil and organic residues, followed by methanol to dissolve any acetone residues left for 2 minutes each. They were then rinsed with deionized (DI) water and blow dried with nitrogen. The substrates were prepared for deposition by ultrasonic seeding in Carbodeon μ Diamond hydrogen terminated nanodiamond aqueous dispersion (2.5 wt.%)

with nanodiamond crystal size ranging from 4.0 to 6.0 nm for 1 minute, immediately followed by DI rinse and blow drying with nitrogen.

3.1.3 Growth Conditions

The seeded samples were loaded in the CVD system on a molybdenum holder mounted on a floating stage. A base pressure of 10^{-7} torr was achieved using a roughening and a turbo pump. Four different series of samples were grown from a hydrogen rich $H_2/N_2/CH_4$ feed gas mixture with 0, 5, 10, and 20% of nitrogen (volume %) in the gas phase which corresponds to flow rates of 0, 10, 20 and 40 standard cubic centimeters per min (sccm) of N_2. The CH_4 flow rate was kept constant at 10 sccm (5% by volume), while the flow rate of N_2 and H_2 was varied to maintain a total flow rate of 200 sccm. Different deposition temperatures were achieved ranging from 1043 K-1295 K by varying the total pressure of the vacuum chamber (between 35-60 torr) and the input microwave power (between 2500-3000 W). The substrate temperature was measured at the interval of every 10 minutes during a growth process of 60 minutes, using an infrared pyrometer with the sensor calibrated at an emissivity value of 0.6.

After each deposition run, the samples were left to cool in nitrogen at ~500 torr for about 10 minutes and then in vacuum for about an hour.

3.2 Sample Analysis

3.2.1 Weight measurement

The seeded Si substrates were weighed before and after deposition using Mettler Toledo XS 105 Scale with 10^{-5} g readability to find the weight of the deposited material. Assuming most of this deposited material to be sp^3 bonded carbon forming diamond grains (the rest being the sp^2 bonded carbon and other defects in the grain boundaries), the density of pure diamond, 3.51g/cm^3 was used to get a rough estimate of the thickness of the material grown using the following relation-

$$Thickness(\mu m) = \frac{\Delta w \cdot 10^4}{A \cdot d} \tag{3.1}$$

where,

Δw = wt. after deposition-wt. before deposition (g)

d = 3.51 g/cm^3

A = surface area of the film (cm^2)

3.2.2 Four-point probe resistivity measurement

Four-point probe method is an electrical impedance measuring technique that uses separate pairs of current-carrying and voltage-sensing electrodes to make more accurate measurements than the simpler and more usual two-terminal sensing. Separation of current and voltage electrodes eliminates the lead and contact resistance from the measurement. This is an advantage for precise measurement of low resistance values.

Current applied via a pair of current or force leads generates a voltage drop across the impedance to be measured according to Ohm's law V=IR. Sense connections are made immediately adjacent to the target impedance using a pair of voltage leads, so that they do not include the voltage drop in the force leads or contacts. Since almost no current flows to the measuring instrument, the voltage drop in the sense leads is negligible. Usually, the sense wires are arranged as the inside pair, while the force wires are the outside pair, otherwise, the accuracy can be affected, because more of the lead resistance is included in the measurement.

Signatone SP4 four-point probe head and HP 4145B Semiconductor Parameter Analyzer with a source voltage of 0.5 V was used to measure and analyze the sheet resistance of the thin films grown. The resistivity was then calculated using the following relation:

$$\rho = R_s \cdot t \cdot 10^{-4} \tag{3.2}$$

where,

ρ = Resistivity (Ωcm),

R_s = Sheet Resistance ($\Omega/\square$),

t = film thickness (μm)

3.2.3 Profilometry

Profilometry is a technique used to extract topographical data from a surface in order to get surface morphology, step heights and surface roughness. Critical dimensions such as step height, curvature, flatness can be computed from the surface topography. There are two types of profilometers: stylus and optical. Stylus profilometers use a probe to detect the surface, physically moving a probe along the surface in order to trace the surface profile. This is done mechanically with a feedback loop that monitors the force from the sample pushing up against the probe as it scans along the surface. Optical profilometry uses light instead of a physical probe to measure the topography.

Dektak 6M profilometer was used to record the surface roughness of the films electro-mechanically by moving the sample beneath a diamond tipped stylus with 5 μm tip radius and a constant stylus force of 15 mg. The stage was set to move the sample at a rate of 6.86 μm/s over a scan length of 480 μm. The roughness of the sample surface, which translates to the vertical motion of the stylus, was measured in terms of arithmetic average deviation from the mean line within the assessment length (R_a) and average height difference between the five highest peaks and five lowest valleys of the scan (R_z).

3.2.4 Raman Spectroscopy

Raman spectroscopy is a technique used to observe vibrational, rotational, and other low-frequency transitions in molecules upon interaction with photons which provide a structural fingerprint by which molecules can be identified. It is a relatively easy, non-destructive, non-contact and quick measurement method and can be performed at room temperature and ambient pressure.

When light is incident upon molecules, most of the photons are scattered elastically, also called Rayleigh scattering such that the scattered photons have the same energy. However, a small fraction of the photons is scattered inelastically, where the energy of the incident photons is either gained or

lost so that the scattered photons are shifted in frequency. Such inelastic scattering is called Raman scattering. Because this frequency modulation is specific to molecular vibration and phonon in crystal, it is possible to analyze composition of material or crystal lattice information by analyzing the spectrum of Raman scattered light.

Typically, a sample is illuminated with a laser beam serving as a source of monochromatic light. Electromagnetic radiation from the illuminated spot is collected with a lens and sent through a monochromator. Elastic scattered radiation corresponding to the Rayleigh scattered photons is filtered out, while the rest of the collected light is dispersed onto a detector. Raman scattered light detected on the shorter wavelength side than Rayleigh scattered light is called anti-Stokes line resulting from an increment in the energy of the incident photon, while that detected on the longer wavelength side is called Stokes line which is due to the loss of energy of the incident photon. In general, Stokes lines with higher intensity are used for analysis.

The information of each dispersed wavelength is converted to wavenumber (1/wavelength) and the difference with the wave number of incident light is plotted on the horizontal axis providing vibrational information of the molecule and the vertical axis represents the intensity of activity. Furthermore, to analyze microscopic areas of the sample, Micro Raman Spectroscopy is used which combines aspects of both the microscope and the Raman spectrometer.

Micro Raman spectra of UNCD films were obtained by using a Horiba Raman spectrometer with 532 nm laser and a grating with a groove density of 1800 lines/mm. A 50× objective lens was used with the optical microscope. The spectra were collected on at least 2 different locations (mostly mid and edge) on the sample from 400 to 3000 cm^{-1} for 30 s accumulated over 1 cycle.

3.2.5 UV-vis Spectroscopy

Ultraviolet-visible spectroscopy refers to absorption or reflectance spectroscopy in part of the ultraviolet and the full, adjacent visible spectral regions, and is routinely used in analytical chemistry for the quantitative determination of different analytes. In this work, relative specular reflectance measurements, where reflectance is calculated from the strength ratio after comparing the light

reflected from the reference sample with the light reflected from the measurement sample, were taken to calculate the thickness of the films. This method of determining thickness is based on the interference patterns observed in N-UNCD submicron films. The maxima and minima positions in the interference patterns detected are shown to be substrate independent, representing the bulk of N-UNCD film and are used in thickness calculations as shown in Eq. (3.3) and (3.4) .

$$d = \frac{\lambda}{4nk} \tag{3.3}$$

$$k = -\frac{1}{1 - \frac{\lambda_k}{\lambda_{k+1}}} \tag{3.4}$$

where,

d = thickness (nm)

λ = maxima or minima position

λ_k,λ_{k+1} = neighboring maximum and minimum positions

n' = refractive index spectrally dependent on the wavelength [46]

k = integer number of a peak/valley, even values of k describe the maxima, and odd the minima

Reflectance measurements were performed using Shimadzu UV-vis 2600 spectrometer in the range 200 to 1200 nm at an incidence angle of 8°. The above relations were used to calculate thickness of each film based on their respective interference patterns.

3.2.6 Scanning Electron Microscopy

Electron microscopy is a method of using an electron beam to form magnified images of specimens. Since the wavelength of electrons is much smaller than the wavelength of light, electrons provide as much as thousand-fold increase in resolving power, i.e. the ability to distinguish between fine details. A scanning electron microscope (SEM) is a type of electron microscope that produces images of a sample by scanning the surface with a focused beam of electrons. The electrons interact with atoms in the sample, producing various signals that contain information about the

surface topography and composition of the sample. The electron beam is scanned in a raster scan pattern, and the position of the beam is combined with the intensity of the detected signal to produce an image.

The interaction of electrons with a sample can result in the generation of many different types of electrons, photons or irradiations. In the case of SEM, the two types of electrons used for imaging are the backscattered (BSE) and the secondary electrons (SE). Backscattered electrons belong to the primary electron beam and are reflected after elastic interactions between the beam and the sample. On the other hand, secondary electrons originate from the atoms of the sample resulting from inelastic interactions between the electron beam and the sample. BSE come from deeper regions of the sample, showing high sensitivity to differences in atomic number, while SE originate from surface regions providing more detailed surface information.

High resolution scanning electron microscopy was performed using a JEOL JSM 7500F with 0.9 nm resolution. Imaging was done at a working distance of 4.5 mm with an accelerating voltage of 5 kV, emission current of 20 μA for the high conductivity samples and 10 μA for the low conductivity samples to minimize charging effects. A secondary electron detector was used to image the surface and cross-section of the films grown.

CHAPTER 4

RESULTS

Ultra-nanocrystalline diamond (UNCD) films were grown at various deposition temperatures for four different nitrogen concentrations in the feed gas mixture resulting in four series of samples referred here as SA, SB, SC and SD for 0, 5, 10 and 20% feed gas N_2 respectively. The following tables (Table 4.1, 4.2, 4.3 and 4.4 for series SA, SB, SC and SD respectively) summarize the resultant properties of each series of films and the values of input parameters used to tune the growth conditions to obtain these films.

The thickness of the films grown is measured by the weight method (t_{weight}) for all the films and UV-vis spectroscopy ($t_{UV\text{-}vis}$) for the films with a measurable interference spectrum. Since $t_{UV\text{-}vis}$ values are more accurate, they are used for resistivity calculations while t_{weight} is used for films for which $t_{UV\text{-}vis}$ could not be calculated. The percentage values of CH_4 and N_2 in the tables refers to the volume percentage of these gases in the feed gas mixture to obtain a total 200 sccm flow rate with the rest of the gas being H_2.

Control of deposition temperature for growth was achieved by varying the input parameters *viz.* the forward microwave power and total pressure in the chamber. An increase in the substrate temperature was observed for a set value of all the input parameters, as nitrogen was increased in the plasma by replacing hydrogen to keep the total gas flow rate constant. Since the only change in the input parameters is the change in partial pressure of nitrogen and hydrogen, the increase in the substrate temperature might be explained in terms of how the energy is transferred from the gas molecules/ions to the substrate. Since N_2 is a heavier molecule compared to H_2, the energy transfer resulting from the bombardment of the molecule with the substrate is more efficient leading to higher substrate temperature.

Sample	**t_{weight} (nm)**	**t_{UV-vis} (nm)**	**Sheet Resistance R_S (kΩ/□)**	**Resistivity (Ωcm)**	**Avg. Roughness R_a (nm)**	**Peak to peak Roughness R_z (nm)**	**Deposition Temperature (Kelvin)**	**Deposition Time (hrs)**	**Total Pressure (sccm)**	**CH_4**	**N_2**	**Forward Power (W)**
SA1	463	499.6	Too high		1.44	8.85	1048	1	40	5%	0%	2500
SA2	659	550.4	$3.5x10^3$	192.64	2.82	20.85	1098	1	45	5%	0%	3000
SA3	657	NA	30.8	2.025	1.66	9.22	1126	1	50	5%	0%	3000
SA4	532	NA	6.4	0.341	1.5	8.14	1156	1	55	5%	0%	3000
SA5	525	NA	0.297	0.015	2.11	10.61	1213	1	57	5%	0%	3000
SA6	687	NA	0.128	0.009	3.19	18.02	1248	1	60	5%	0%	3000

Table 4.1: Series SA films grown with 0% N_2 concentration

Sample	**t_{weight} (nm)**	**t_{UV-vis} (nm)**	**Sheet Resistance R_S (kΩ/□)**	**Resistivity (Ωcm)**	**Avg. Roughness R_a (nm)**	**Peak to peak Roughness R_z (nm)**	**Deposition Temperature (Kelvin)**	**Deposition Time (hrs)**	**Total Pressure (sccm)**	**CH_4**	**N_2**	**Forward Power (W)**
SB1	456	393.52	$15x10^3$	590.2	4.2	19.34	1043	1	35	5%	5%	2500
SB2	541	528.9	$5x10^3$	264.4	4.47	24.61	1085	1	40	5%	5%	2500
SB3	498	518.4	12.56	0.65	4.83	18.78	1103	1	40	5%	5%	2700
SB4	636	584.37	20.63	1.2055	1.88	13.55	1118	1	45	5%	5%	2500
SB5	595	539.5	20.5	1.106	1.7	12.02	1125	1	45	5%	5%	2700
SB6	479	NA	3.76	0.1803	1.83	14.9	1148	1	43	5%	5%	3000
SB7	481	NA	5.29	0.2544	4.51	21.6	1151	1	45	5%	5%	3000
SB8	453	NA	2.74	0.124	2.09	9.93	1163	1	50	5%	5%	3000
SB9	532	NA	0.17	0.009	2.76	14.79	1229	1	60	5%	5%	3000

Table 4.2: Series SB films grown with 5% N_2 concentration

Sample	**t_{weight} (nm)**	**$t_{UV\text{-}vis}$ (nm)**	**Sheet Resistance R_s (kΩ/□)**	**Resistivity (Ωcm)**	**Avg. Roughness R_a (nm)**	**Peak to peak Roughness R_z (nm)**	**Deposition Temperature (Kelvin)**	**Deposition Time (hrs)**	**Total Pressure (sccm)**	**CH_4**	**N_2**	**Forward Power (W)**
SC1	391	344.69	$4x10^3$	137.87	2.13	19.02	1068	1	35	5%	10%	2500
SC2	500	484.13	42.9	2.077	2.68	20.51	1101	1	40	5%	10%	2500
SC3	627	595.27	50.38	2.999	2.27	22.7	1145	1	45	5%	10%	2700
SC4	497	513.58	13.5	0.69	1.88	16.72	1163	1	45	5%	10%	3000
SC5	517	NA	0.66	0.034	2.39	12.17	1223	1	55	5%	10%	3000

Table 4.3: Series SC films grown with 10% N_2 concentration

Sample	**t_{weight} (nm)**	**$t_{UV\text{-}vis}$ (nm)**	**Sheet Resistance R_s (kΩ/□)**	**Resistivity (Ωcm)**	**Avg. Roughness R_a (nm)**	**Peak to peak Roughness R_z (nm)**	**Deposition Temperature (Kelvin)**	**Deposition Time (hrs)**	**Total Pressure (sccm)**	**CH_4**	**N_2**	**Forward Power (W)**
SD1	194	223.16	$30x10^3$	669.48	2.44	21.51	1115	1	35	5%	20%	2500
SD2	279	239.66	$12x10^3$	287.6	2.13	18.61	1138	1	40	5%	20%	2500
SD3	371	325.31	$2x10^3$	65.06	2.81	21.01	1195	1	45	5%	20%	3000
SD4	367	398.96	19.7	0.786	3.53	27.86	1220	1	50	5%	20%	3000
SD5	552	NA	8.36	0.46	3.15	18.5	1259	1	55	5%	20%	3000
SD6	479	NA	4.7	0.225	2.79	18.9	1263	1	60	5%	20%	3000
SD7	365	NA	1.45	0.053	2.56	14.73	1295	1	65	5%	20%	3000

Table 4.4: Series SD films grown with 20% N_2 concentration

4.1 Resistivity

The room temperature resistivity of the films as a function of deposition temperature is shown in Fig. 4.1. Deposition temperature (T_d) here refers to the substrate temperature measured with an optical pyrometer. A variation of about $\pm$10K (e_1) was observed based on different viewing angles along with a temperature variation of about $\pm$5K (e_2) during the one hour growth of each film. A resultant error bar of $\pm$11.18K $(e_1^2 + e_2^2)^{1/2}$ for the x-axis is thus calculated taking both these variations into account.

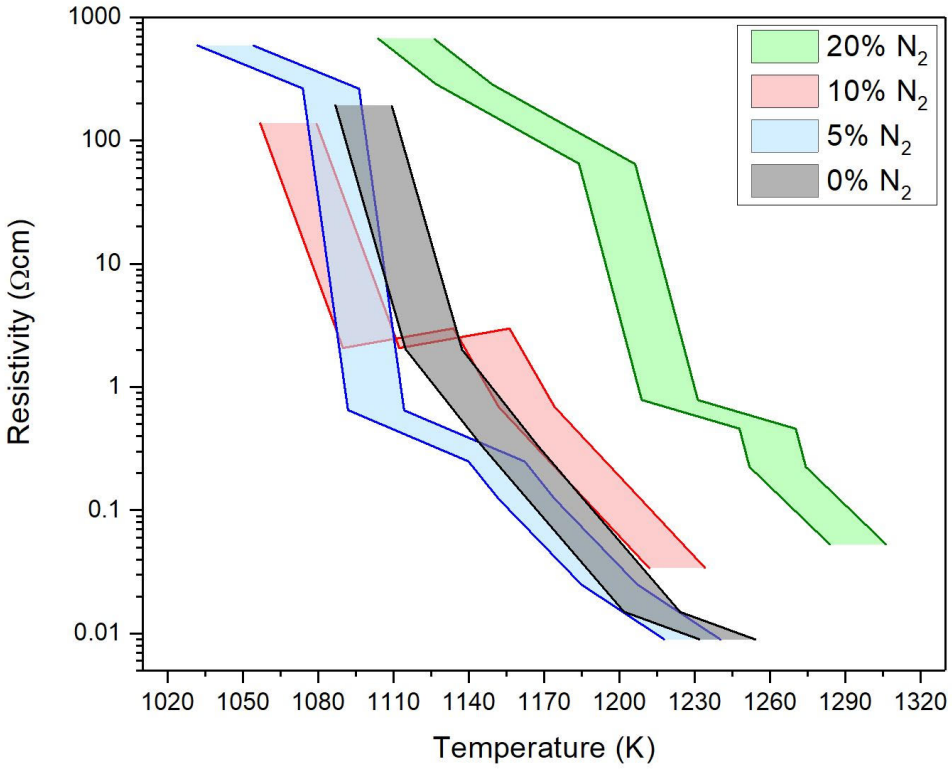

Figure 4.1: Resistivity of all the films of series SA, SB, SC and SD as a function of deposition temperature

Fig. 4.1 presents a direct comparison of resistance tunability for undoped and nitrogen incorporated UNCD films resulting from a range of T_d. The resistivity decreases exponentially by more than four orders of magnitude from 10^2 to 10^{-2} Ωcm as T_d increases over a range of 250 K for various concentrations of nitrogen in the plasma, including the undoped samples. The exponential decay and the lowest resistivity measured corresponding to a conductivity value of 100 $\Omega^{-1}cm^{-1}$

is in accordance with previously reported values for N(UNCD) where the trend was seen independently for two different deposition configurations- 1) for increasing nitrogen concentration (0 to 20%) in the plasma with a constant deposition temperature [32, 38] and, 2) for increasing deposition temperature with constant nitrogen concentration in the plasma [41, 40].

While the trend and resistivity values recorded here are in accordance with the increasing T_d configuration for a constant amount of nitrogen in the plasma, it is not the same for the increasing nitrogen configuration. It can be seen from the graph in Fig. 4.1 that for a given T_d, the resistivity value does not change as much with nitrogen as it changes with T_d and it in fact increases with increasing nitrogen content as opposed to previous findings [32, 38].

To understand the factors responsible for the achieved resistance tunability, the changes in the structure of the film based on different growth parameters are discussed in the following sections based on the results obtained from Raman spectroscopy and SEM images of the film.

4.2 Analysis of Raman Spectra

The Raman spectra collected for all the four series of films grown with various nitrogen concentrations exhibit some prominent features described as follows- 1) A band with the peak position ranging between 1333 cm^{-1} and 1350 cm^{-1}. The 1333 cm^{-1} peak is the characteristic diamond peak attributed to sp^3 bonded carbon. The 1350 cm^{-1} feature appears for graphitic materials in the form of a band induced by the defect or disorder in the sp^2 bonded carbon. Polycrystalline graphite exhibits D band in its spectrum due to the outer rim of graphite crystallites which tends to have more defects as opposed to the inside of the graphite crystal for which the band is not present [47].

In this discussion, this band will be referred as the D band as has been used traditionally for systems containing mixed phases of sp^2 and sp^3 bonded carbon.

2) A band with the peak position ranging between 1545 cm^{-1} and 1590 cm^{-1} which can be recognized as the G band. In addition to the D band, graphitic materials also exhibit a band at 1588 cm^{-1} called the G band attributed to the crystalline graphitic structure with sp^2 bonded carbon. The integrated intensity ratio of the D and G bands, I(D)/I(G) is directly proportional to the defect quantity in

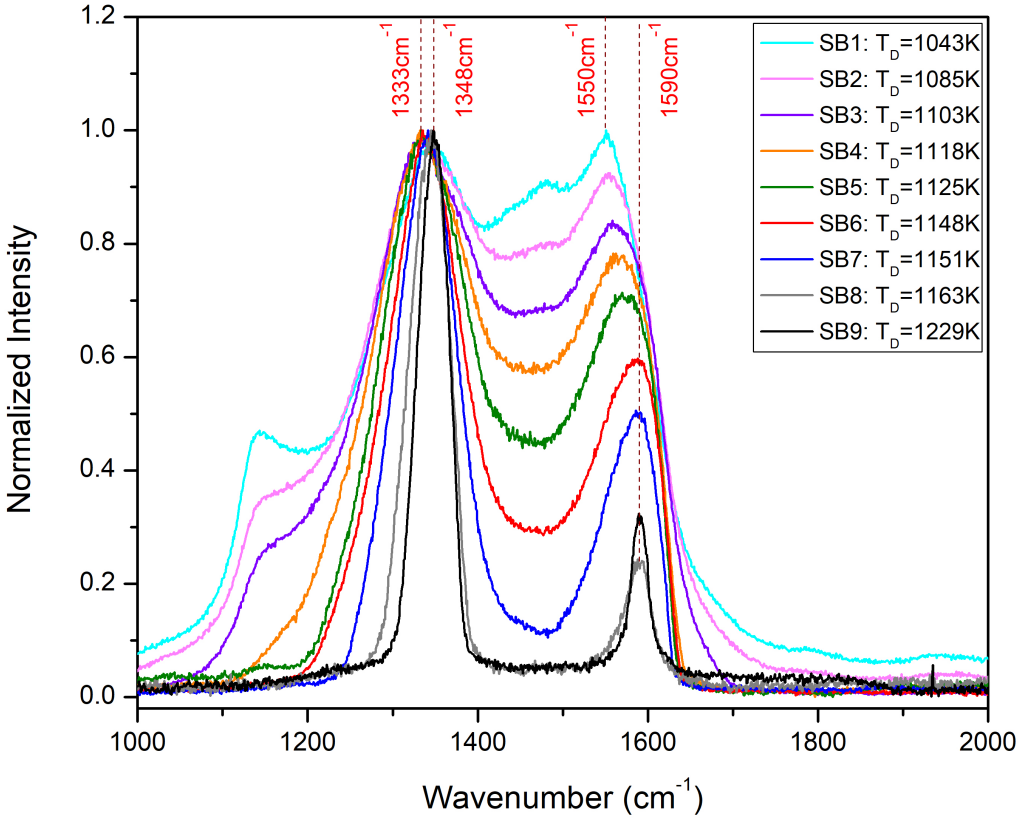

Figure 4.2: Raman spectra for 5% N_2 samples as a function of T_d

graphitic materials and inversely proportional to the in-plane crystallite size.

3) A shoulder at 1140 cm^{-1} and a weak peak at 1480 cm^{-1} representing ω_1 and ω_3 modes of trans-polyacetylene (t-PA) chains respectively.

The Raman spectra studied both as a function of T_d and N_2 concentration in the feed gas mixture show various trends in the position, intensity and shape of the peaks discussed as follows.

4.2.1 Raman spectra as a function of T_d

Fig. 4.2 shows the Raman spectra of films from SB series, grown with 5% N_2 in the feed gas mixture for various T_d. As the temperature increases, the G band peak shifts from 1550 cm^{-1} to 1590 cm^{-1} with decreasing intensity which shows a reduction of the amorphous carbon content and

a conversion from short-range to long range order of sp^2 bonded carbon [48]. The peak shift is also accompanied by its narrowing indicating an increase in the crystallinity of the material. Thus, with the increase in T_d, the sp^2 bonded carbon changes from amorphous to polycrystalline graphite. The high intensity of defect induced D band with respect to G band can be attributed due to a large volume of crystallite edges resulting from small crystallite size. The size of these crystallites is in nanometer scale as confirmed by SEM images in the next section.

For lower T_d, the D band is quite broad with its peak at 1333 cm^{-1}. As T_d increases, the band gets narrower and the peak position stays constant up to 1148 K. The film grown has a mixture of sp^2 and sp^3 bonded carbon forming a matrix of diamond grains surrounded by grain boundaries, identified as ultra-nano crystalline diamond (UNCD) based on the SEM images (shown in the next section). As T_d is increased beyond 1148 K, the D band continues to get narrower and the peak at 1333 cm^{-1} jumps to 1350 cm^{-1}, indicating that there is very less or no amount of sp^3 bonded carbon to be detected by Raman spectroscopy which is more sensitive towards the detection of sp^2 bonded carbon. A complete shift of the 1333 cm^{-1} peak to 1350 cm^{-1} peak at higher temperatures showing a material change of diamond to graphite is normal expect due to the existence of fundamental phase transition at 1500 K from metastable diamond structure to its fundamental ground state which is graphite. The phenomenon of diamond being damaged or changed into other carbon structures when exposed to high temperatures, is also in agreement with previous results [41, 49].

The features at 1140 cm^{-1} and 1480 cm^{-1} de-intensify as T_d increases and completely disappear after 1103 K due to the release of hydrogen at increased temperatures. The two peaks were recognized as characteristic signatures of nanocrystalline diamond until it was realized that they resemble the behavior of the ω_1 (in-plane C-H bending combined with C-C stretching) and the ω_3 (C=C stretching) vibration modes of trans-polyacetylene (t-PA). Accordingly, these features were associated with fragments of t-PA-like species also present in the grain boundaries. The disappearance of these features due to annealing also confirms that these modes of t-PA are not related to diamond grains [50].

Fig.4.3, 4.4 and 4.5 show the Raman spectra as a function of T_d for SA, SC and SD series of

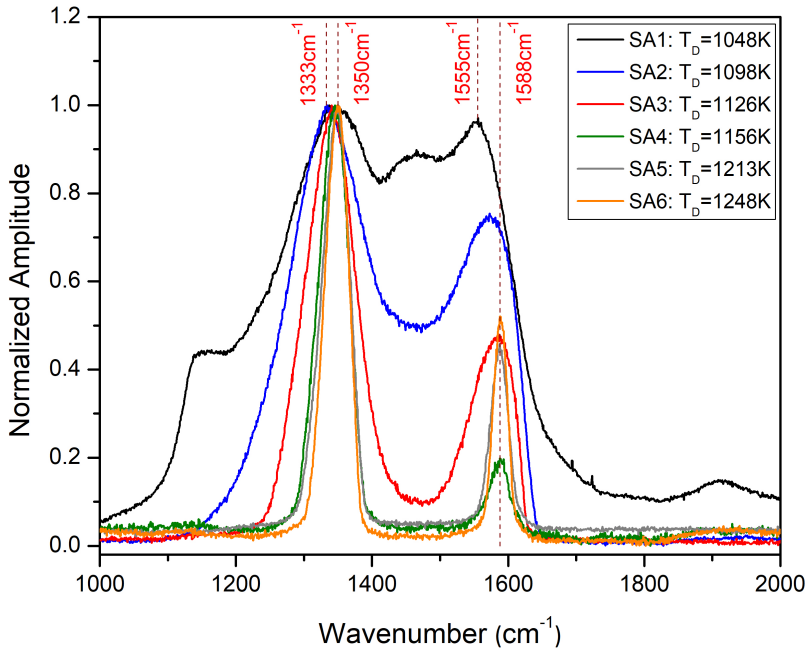

Figure 4.3: Raman spectra for 0% N_2 samples as a function of T_d

films grown with 0, 10, 20% feed gas N_2 respectively. The trends in the features of Raman spectra are very consistent with increasing T_d irrespective of the concentrations of nitrogen in the plasma. The trends common to all the four series of films can be summarized as follows-

1) The shift in the D band peak from 1333 cm^{-1} to 1350 cm^{-1} along with the narrowing of the band with increasing T_d.

2) The decrease in the intensity and the shift in the G band peak from 1550 cm^{-1} to 1590 cm^{-1} along with the narrowing of the band with increasing T_d.

3) The decrease in the intensity of the t-PA features at 1140 cm^{-1} and 1480 cm^{-1} till they completely disappear as T_d increases. These features disappear after about 1100 K for all the four series of films which again confirms that these are not related to diamond. It also confirms the consistency of the pyrometer temperature measurements. The removal of t-PA chains present in the grain boundaries also enables the formation of better sp^2 bonded carbon phase in the grain boundaries in all four series of films.

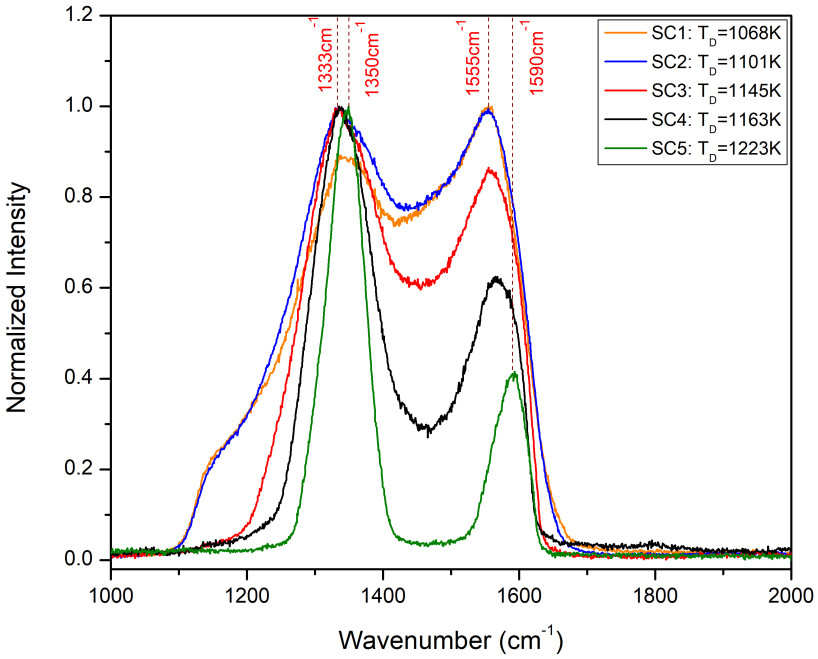

Figure 4.4: Raman spectra for 10% N_2 samples as a function of T_d

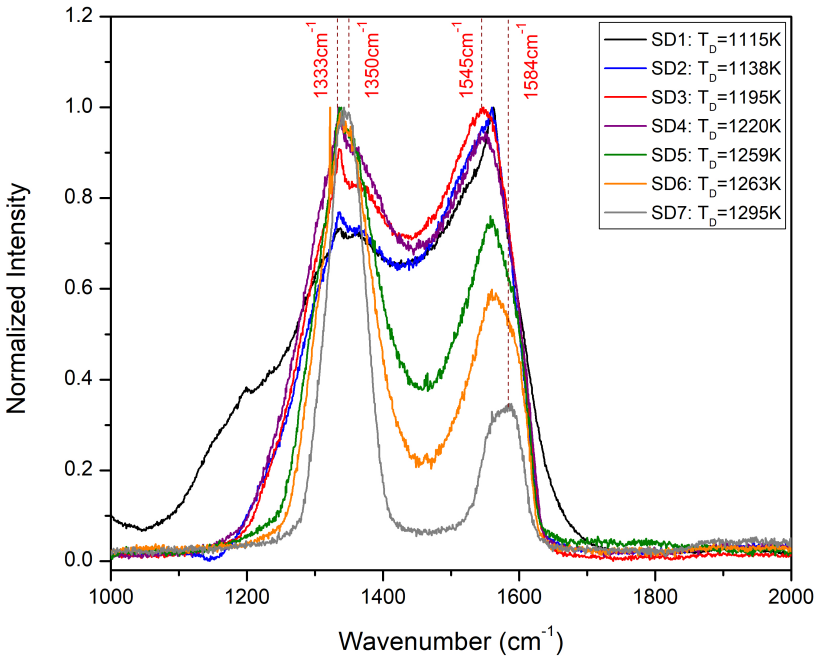

Figure 4.5: Raman spectra for 20% N_2 samples as a function of T_d

Thus, in all 4 series of experiments, there was a consistent and reproducible material transformation from UNCD to nanocrystalline graphite.

The films of series SD grown with 20% feed gas N_2 show an additional feature in the D band as can be seen in Fig. (20% N2). The D band has two peaks at 1333 cm^{-1} due to sp^3 bonded carbon and at 1364 cm^{-1} due to disordered sp^2 bonded carbon. The 1333 cm^{-1} peak keeps intensifying with respect to the 1364 cm^{-1} peak as T_d increases upto 1259 K after which the peaks merge together and shift completely to 1350 cm^{-1} at 1295 K. The appearance of the 1333 cm^{-1} peak separately confirms that the film consists of a mixture of sp^3 bonded crystalline carbon and sp^2 bonded disordered carbon.

4.2.1.1 Graphitization

The change in the peak positions and width of the D and G bands has been noted for all the four series of films which indicate a material transition from diamond grains embedded in amorphous carbon matrix to nanocrystalline graphite. To confirm the process of graphitization in the films, T_d was increased further for the 0% N_2 films. Fig. 4.6 shows the comparison between the Raman spectra of 0% N_2 films grown at high T_d, single crystal diamond (SCD) sample with peak at 1333 cm^{-1} and highly ordered pyrolytic graphite (HOPG) sample with peak at 1582 cm^{-1}. The intensity of G band peak at 1550 cm^{-1} of the 0% N_2 films keeps decreasing owing to the decrease in the amorphous content in the film along with the shift of the peak position from 1550 cm^{-1} to 1588 cm^{-1} as evident from Fig. 4.3.

When the peak has completely shifted to 1588 cm^{-1}, it doesn't change its position any further with an increase in T_d beyond 1156 K and starts intensifying as shown in Fig. 4.6. The increase in the 1588 cm^{-1} peak shows an increase in the amount of crystalline form of sp^2 bonded carbon. The absence of the diamond peak and the presence of both D and G bands in the spectra of 0% N_2 films as opposed to just a G band from HOPG sample confirms that now the material grows completely as nanocrystalline graphite. The increase in the crystalline form of sp^2 bonded carbon is also evident from Fig. 4.2 for the 5% N_2 films where G band peak completely shifts to 1590 cm^{-1}

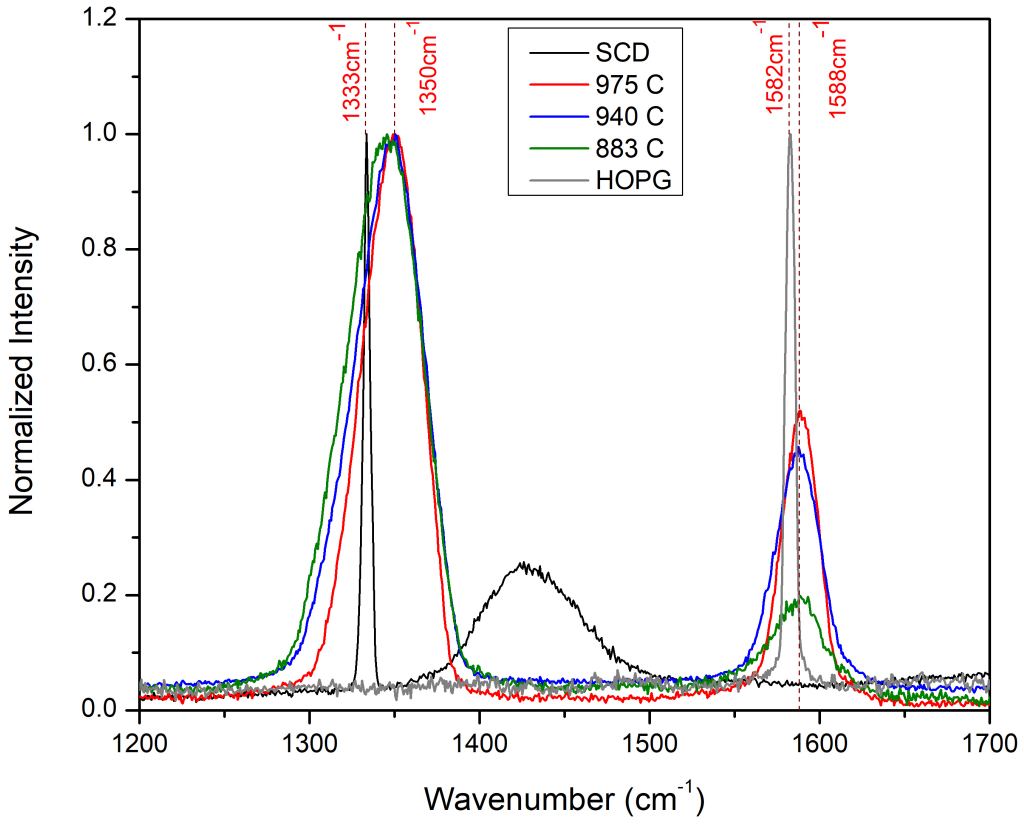

Figure 4.6: Comparison of Raman spectra of highly graphitized films with single crytsal diamond and highly oriented pyrolytic graphite

at 1163 K and starts intensifying for higher T_d.

A similar material transition was also observed in our study of glow plasma discharge during field emission from UNCD cathodes used as emitters [51]. Data from SEM and Raman show the conversion of nano diamond to nano graphite caused by the electron emission self-induced heating of the emitter to 3000-4000 K. Fig. 4.7 compares the Raman spectra of the cathode before and after the damage due to heating. It shows that the damaged areas, denoted by the dark spots in the inset image, exhibit the Raman characteristics of nano graphite.

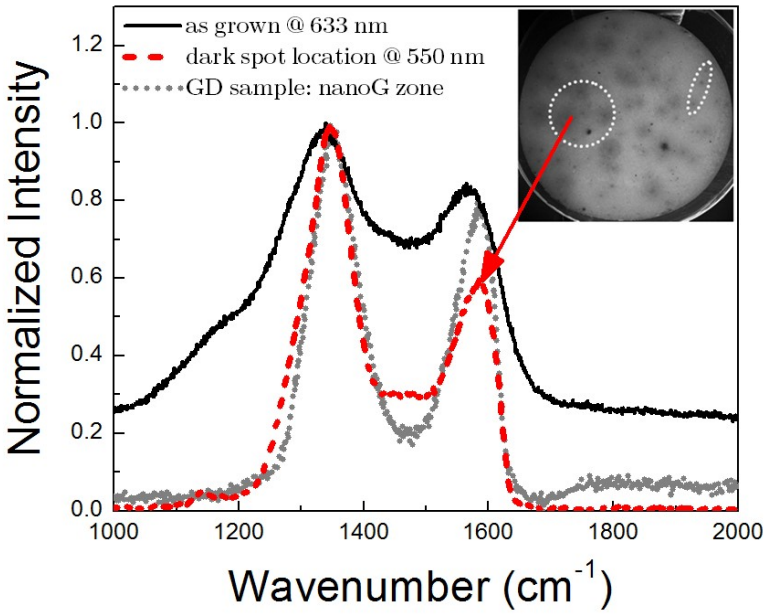

Figure 4.7: Raman spectra for graphitic and UNCD sites on the damaged (a) and pre-damaged (b) cathodes due to electron field emission.

4.2.2 Raman spectra as a function of N_2 concentration in the feed gas

Fig. 4.8 and 4.9 show a comparison of Raman spectra of films with varying nitrogen concentration deposited at 1098 K and 1126 K respectively. A comparison of the peak position and intensity of the G band shows that the amount of amorphous sp^2 bonded carbon increases with increasing feed gas N_2 concentration for films deposited at a constant T_d. This can be explained by the amount of energy required in the formation of increasing amount of CN bonds in the films with increasing nitrogen content in the plasma. The positive enthalpy of formation of CN bonds makes the incorporation of nitrogen in the films endothermic. Thus, the available thermal energy gets distributed between the incorporation of nitrogen through the formation of CN bonds in the grain boundary of the films and the conversion of amorphous sp^2 carbon to crystalline form. This accounts for the increased amount of amorphous sp^2 carbon detected in high nitrogen concentration films.

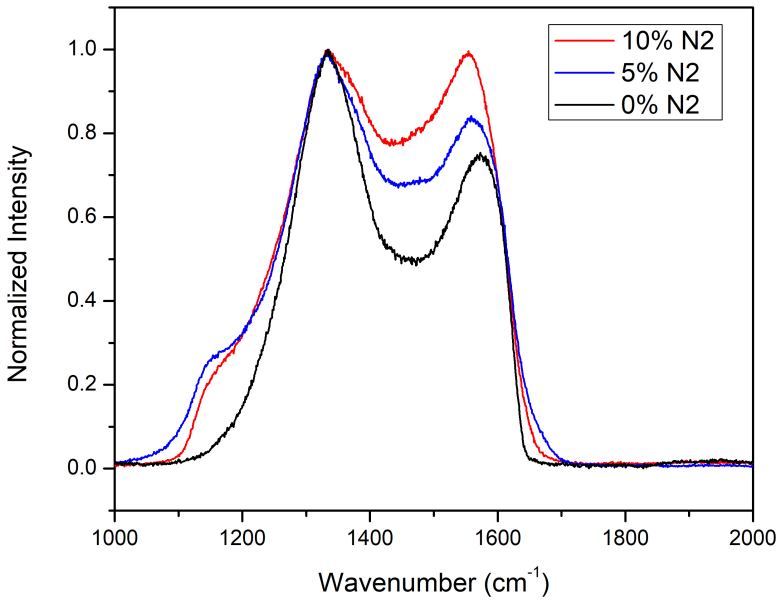

Figure 4.8: Raman spectra for samples deposited at 1098 K with 0, 5 and 10% N_2 concentration

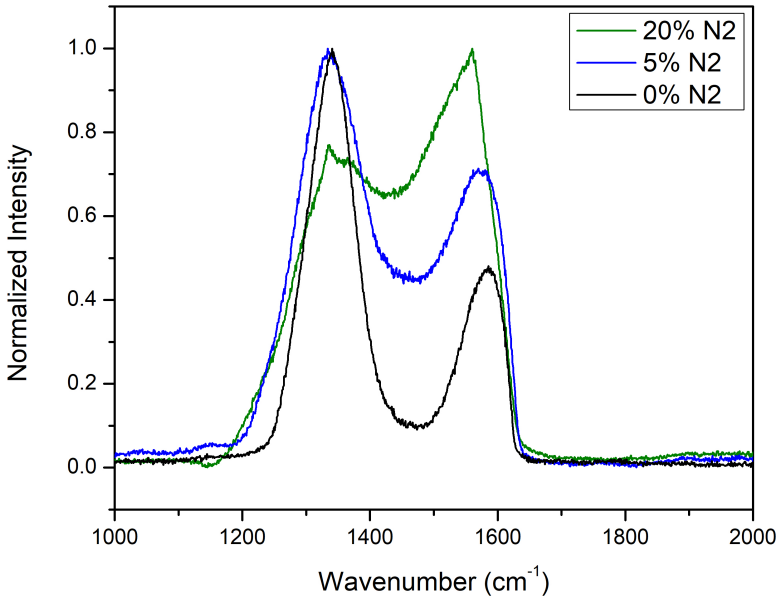

Figure 4.9: Raman spectra for samples deposited at 1126 K with 0, 5 and 20% N_2 concentration

It also explains the increase in resistivity of the films with increasing feed gas nitrogen concen-

tration for a given T_d, as shown in Fig. 4.1. An upward shift in the required deposition temperature is observed to get UNCD films with similar resistivities for increasing nitrogen content in the plasma. For instance, the resistivity value of 0.6 Ωcm was achieved at 1103 K with 5% N_2 as opposed to 1163 K for 10% N_2 and 1221 K for 20% N_2. Increasing CN bond formation for the incorporation of nitrogen leads to an overall increase in the required thermal energy to achieve the same level of crystallinity of sp^2 bonded carbon which is the major contributing factor towards the conductivity of the films.

The incorporation of nitrogen in the films with increasing feed gas nitrogen concentration has been reported to saturate at $2x10^{20}$ cm^{-3} but the value of feed gas nitrogen concentration at which saturation occurs is not consistent in literature [32, 39, 40]. The values were calculated from SIMS measurements which does not accurately resolve changes in value smaller than an order of magnitude. XPS spectra for N-UNCD films shows a slight increase in the N 1s peak but due to low signal to noise ratio, this change is not properly resolved [40]. These reports make the argument of saturation of incorporated nitrogen debatable. Here, we assume that the nitrogen incorporation does not saturate and the increase is too small to be detected by traditional methods.

4.2.3 Resistivity as a function of G band peak position

The mechanism of resistance tunability with varying nitrogen concentrations can be explained using Fig. 4.10 which shows resistivity as a function of G peak position between 1550 cm^{-1} to 1590 cm^{-1}, for various nitrogen concentrations in the feed gas. As the G peak position at 1550 cm^{-1} corresponds to amorphous phase of sp^2 bonded carbon, a lower value of G peak position corresponds to a lower amount of crystalline sp^2 carbon phase which is responsible for conduction. Films corresponding to higher feed gas N_2 content can obtain a particular value of resistivity with a lower G peak position, i.e., with lower crystallinity of the sp^2 bonded carbon, as compared to the films corresponding to lower feed gas N_2 content with higher crystallinity of the sp^2 bonded carbon. Thus the amount of feed gas N_2 is another factor that affects conductivity apart from the extent of crystallinity of the sp^2 bonded carbon.

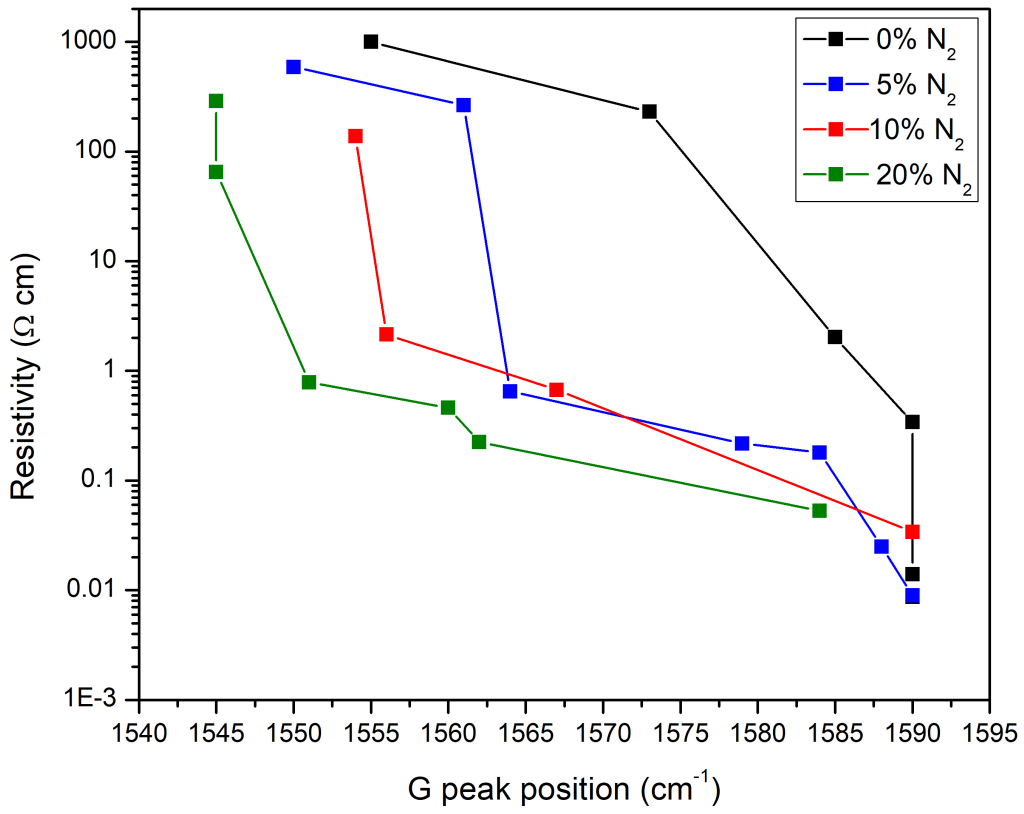

Figure 4.10: Resistivity as a function of G peak position

Addition of nitrogen in the feed gas leads to the incorporation of nitrogen in the grain boundaries which increases the amount of sp^2 bonded carbon due to the increase in the volume of grain boundaries. This results to better spatial connectivity of sp^2 bonded carbon, thus, enhancing the conductivity of the film. This leads to increased conductance of the higher nitrogen concentration films grown at low T_d with lower crystallinity of the sp^2 bonded carbon. This provides us with the ability to tune the resistivity of the UNCD films without transforming it a more graphitic material.

As T_d increases, the crystallinity of sp^2 carbon increases along with increased graphitization of the film, which leads all the four series of films to move towards lower resistivity value and converge at the same G peak position at 1590 cm^{-1}, irrespective of the feed gas nitrogen concentration.

4.3 Analysis of SEM images

Electron imaging of the surface of the films shows the growth of ultra-nanocrystalline diamond with strong morphology changes for varying deposition temperatures and nitrogen concentrations.

4.3.1 Surface Morphology

Fig. 4.11, 4.12, 4.13 and 4.14 show the surface morphology of films with increasing T_d for 0, 5, 10 and 20% N_2 respectively.

4.3.1.1 Changes in surface morphology with varying T_d

Comparison of the morphology of films grown at a particular nitrogen concentration shows a transition from UNCD to nanocrystalline graphite with increasing T_d. Films grown at lower T_d as shown in Fig. 4.11(a), 4.12(a), 4.13(a) and 4.14(a) exhibit densely packed nanometer sized grains forming a continuous film and thus, confirming the growth of UNCD films. At higher deposition temperatures, it is seen in the SEM images, and as already indicated by the Raman spectroscopy, that the amount of deposited graphite increases. Fig. 4.11(b), 4.12(b), 4.13(b) and 4.14(b) show the appearance of small voids as T_d increases. These voids grow wider with further increase in T_d and the morphology now looks like a layer of graphite flakes as seen in Fig. 4.11(c), 4.12(c), 4.13(c) and 4.14(c). This is in accordance with the transition in morphology from densely packed nano-diamond film to flakes of graphite with increasing T_d reported earlier [49].

4.3.1.2 Changes in surface morphology with increasing N_2 concentration

Films grown at lower T_d show a change in the grain size as nitrogen concentration is varied. For low N_2 concentration (Fig. 4.11(a), 4.12(a) for 0%, 5% nitrogen respectively), the morphology of the films remains largely unchanged. Fig. 4.13(a) shows a slight increase in the grain size for 10% N_2 film. However, grain size increases significantly and form clusters for the 20% N_2 film as seen in Fig. 4.14(a) while still lying in the ultra-nano scale range.

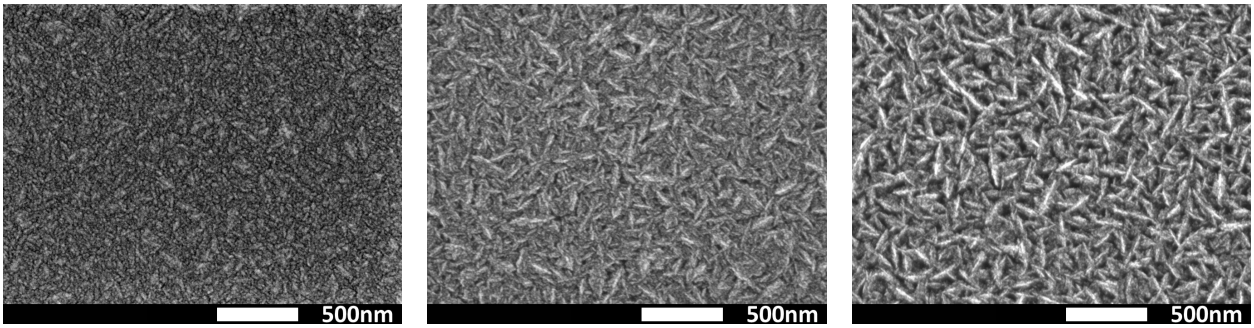

(a) SA1: T_d=1048 K (b) SA3: T_d=1126 K (c) SA4: T_d=1156 K

Figure 4.11: SEM images of samples grown with 0% N_2 concentration

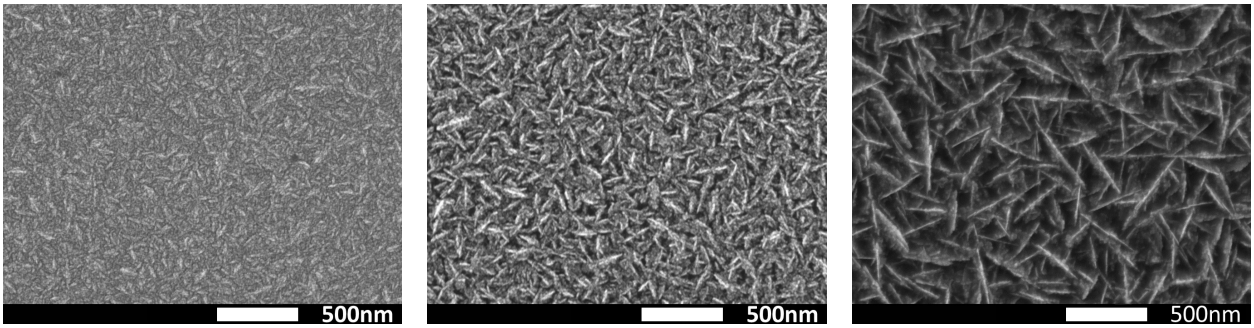

(a) SB1: T_d=1043 K (b) SB7: T_d=1080 K (c) SB9: T_d=1229 K

Figure 4.12: SEM images of samples grown with 5% N_2 concentration

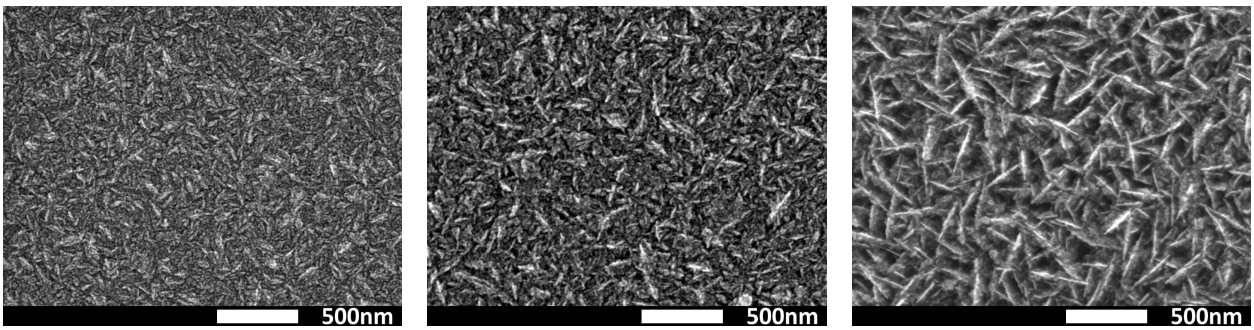

(a) SC2: T_d=1101 K (b) SC4: T_d=1163 K (c) SC5: T_d=1223 K

Figure 4.13: SEM images of samples grown with 10% N_2 concentration

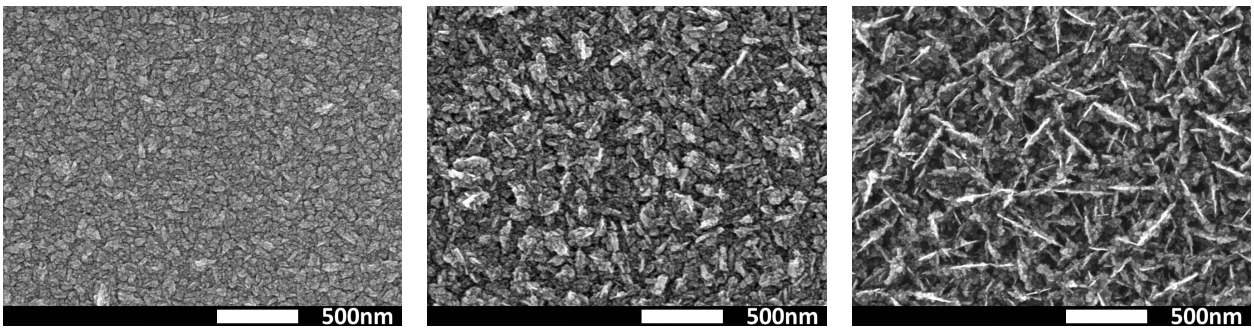

(a) SD1: T_d=1115 K (b) SD4: T_d=1120 k (c) SD7: T_d=1295 K

Figure 4.14: SEM images of samples grown with 20% N_2 concentration

These results are in accordance with previously reported changes in grain size with varying nitrogen concentration [32, 31].

4.3.2 Bulk Morphology

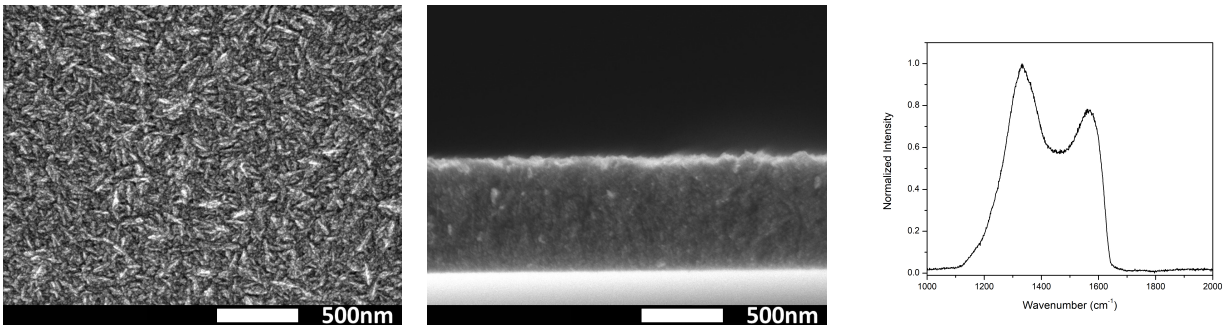

(a) Top view (b) Cross-section (c) Raman spectrum

Figure 4.15: SEM and Raman spectrum of sample: SB4, grown with 5% N_2

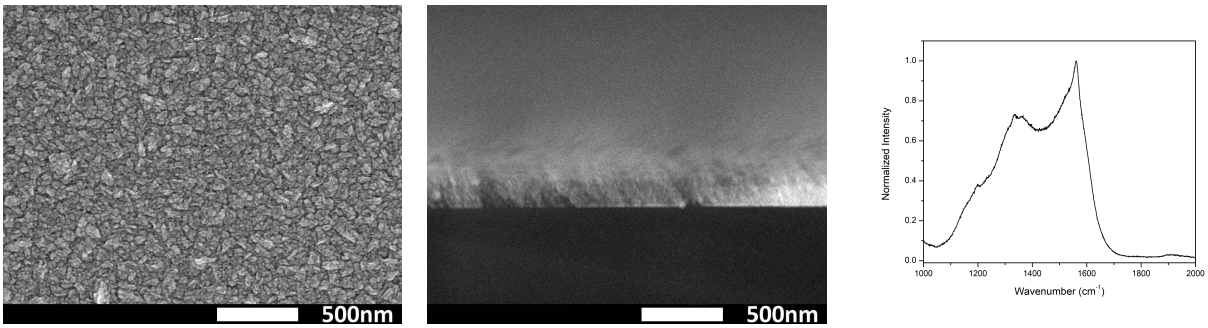

(a) Top view (b) Cross-section (c) Raman spectrum

Figure 4.16: SEM and Raman spectrum of sample: SD1, grown with 20% N_2

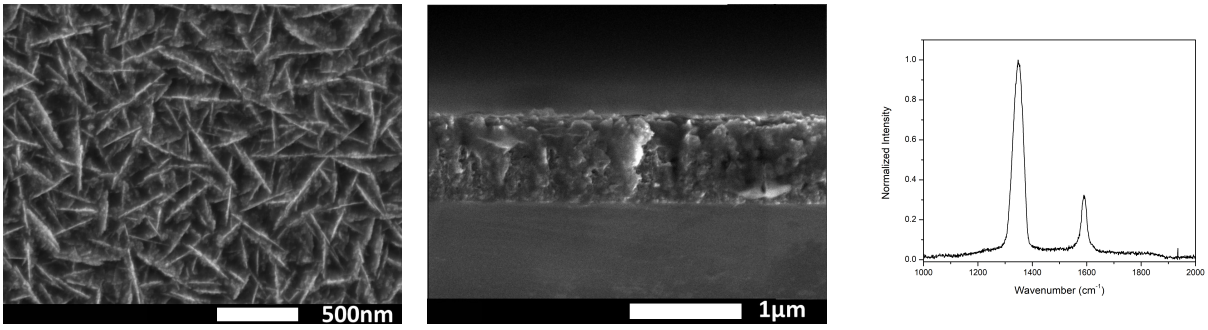

(a) Top view (b) Cross-section (c) Raman Spectrum

Figure 4.17: SEM and Raman spectrum of sample: SB9, grown at high T_d

The cross-sectional view of the films grown at lower T_d shows an absence in an identifiable columnar structure for both low and high nitrogen concentration samples, however, there is significant difference between the low and high nitrogen concentration samples owing to varying grain sizes.

The cross-section of 5% N_2 films in Fig. 4.15(b) shows smooth fracture surfaces which suggest that the nanocrystalline diamond does not grow from the initial nulclei at the substrate-film interface but is the result of very high renucleation rates [27]. This results in a highly dense continuous film with no discernable growth morphology as the crystallite sizes are too small as seen in Fig. 4.15(a) to be resolved in the cross-sectional view. The cross-section of 20% N_2 films in Fig. 4.16(b) also shows a highly dense film resulting from high renuclation rate along with discernable grains due to larger crystallite size as seen in Fig. 4.16(a). Fig. 4.17(b) shows the cross-sectional view of highly graphitized film grown at high T_d in which the crystallites of graphite are loosely packed in the form of flakes.

4.4 Reflectance Spectrum

A comparison of the reflectance spectrum obtained from UV-vis spectroscopy of samples grown at low and high T_d is shown in Fig. 4.18. High reflectance and strong interference pattern is exhibited by sample SB1 deposited at 1043 K which shows the highly reflective characteristic of diamond (as can be seen from the bright pink color of the film) retained in the film. As T_d increases, the reflectance from the film decreases and the interference pattern grows weaker to a point where it is almost negligible due to high optical absorption of the graphitized samples. This can be seen for the highly graphitized sample SB9 grown at 1229 K with the inset image showing the highly absorptive black color of the film..

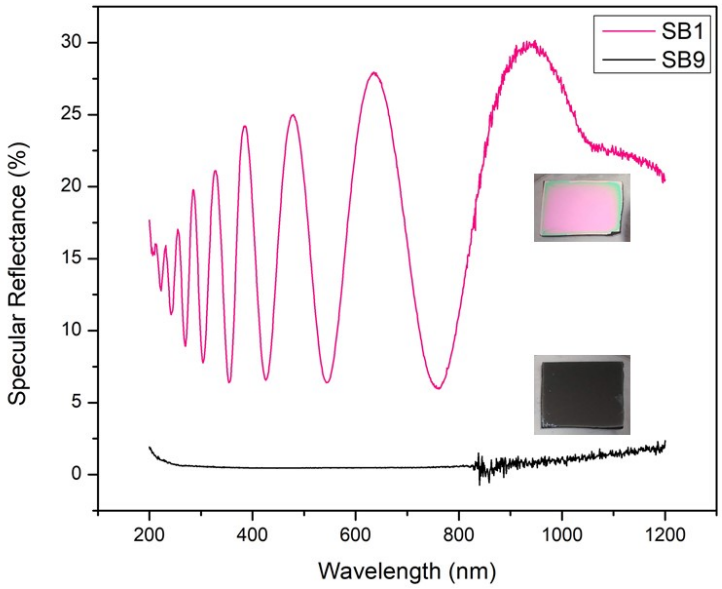

Figure 4.18: Comparison of reflectance spectra of UNCD and highly graphitized film

4.5 Thickness

The thickness of the films was measured using two different methods independently, to cross-verify the calculated values from each method. Thickness calculation from the weight measurement method was done using the density of pure diamond and that from UV-vis spectroscopy using the wavelength dependent refractive index of pure diamond. Difference of up to ~50 nm was found between the calculated values from the two methods. Thickness could not be calculated using UV-vis spectroscopy for the highly graphitized samples due to very weak to negligible interference patterns obtained. These values of thickness were also compared with the thickness observed from the SEM images of the cross-section of the films (comparison shown in Fig. 4.19). The calculated values were close to the observed values from SEM images for the low temperature samples (Samples 1 and 2), thus confirming they have properties close to pure diamond. For the higher temperature samples, the difference between the SEM observed and calculated values increases. For the highest temperature sample, this difference is maximum (Samples 3 and 4).

The SEM observed value of this sample rather matches with the value calculated from the weight difference method by substituting the density of diamond (3.51 g/cm^3) with the density of graphite (2.27 g/cm^3). This gives a fundamental proof of material transition from UNCD to nanocrystalline graphite as interpreted by the Raman spectra (shown alongside and discussed before) and SEM images of the top-view of the films.

SAMPLE#	THICKNESS (nm)		
	SEM	Density of diamond (3.51 g/cm^3)	Density of graphite (2.27 g/cm^3)
Sample 1	156	194	300
Sample 2	764	636	983
Sample 3	742	517	799
Sample 4	830	532	822

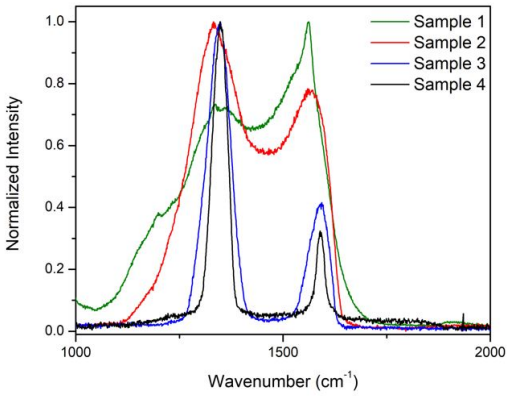

Figure 4.19: Confirmation of graphitization through thickness measurement

4.6 Defining UNCD based on Raman spectra

Raman spectroscopy reveals and traces the bonding structure of the films under study which undergoes striking changes as T_d increases. Namely, the change in the peak positions and widths of D and G bands indicate a clear material phase transition from diamond grains lined with initially amorphous carbon GB to nanocrystalline graphite. The film remains to be UNCD as long as it has diamond grains indicated by the presence of 1333 cm^{-1} peak and sp^2 grain boundaries in mixed amorphous/crystalline state with G band peak located somewhere between 1550 cm^{-1} and 1590 cm^{-1}. The material transforms completely to nanocrystalline graphite when the D band completely shifts to nearby wavenumber 1350 cm^{-1} and therefore no longer exhibits diamond content in the film but rather represents nanographite defect.

CONCLUSION

Undoped and nitrogen incorporated ultra-nanocrystalline diamond films were successfully grown in a systematical manner using microwave plasma assisted chemical vapor deposition at various deposition temperatures for 0, 5, 10 and 20% N_2 concentrations in the feed gas of 1% CH_4/H_2 mixture. Resistivity of the films was found to decrease exponentially by over four orders of magnitude with increasing deposition temperature for all the four nitrogen concentration films, including the nitrogen-free ones. For all the films, Raman and SEM analysis revealed a consistent and reproducible material transformation of the material from UNCD to nanocrystalline graphite with increasing deposition temperature. We found that

(*i*) the GB size effects leading to their enhanced connectivity (enhanced number of contacts) within the GB network promoted by addition of nitrogen; and

(*ii*) improved crystallinity of individual GBs promoted by the elevated deposition temperature;

are equally important in fundamental understanding of conductivity mechanism in UNCD and have to be taken into account along with energy space (density of states band diagram) considerations. Practically speaking, our results outline pathways for engineering resistivity in UNCD films toward targeted electronics applications.

Beyond that, we revisited the basic definition of UNCD material as it was not fully addressed in the previous experimental literature.

Ultimately, we find that sp^2 phase plays primary role in setting UNCD conductivity. This is evidenced by the fact that, unlike in Bhattacharya *et al*., even undoped samples had high conductivities and ultimately reached the champion metrics of ~100 S/cm when fully graphitized. The most recent results [43, 41] are consistent with our conclusion. In the context of redefined term UNCD and actual mass density evaluation, the most conductive films for all N2 concentrations studied are no longer UNCD. There is one important difference between 0% and 20 % series, though. Thanks to initially enhanced connectivity of GBs, 20 % series retain UNCD bonding toward the highest deposition temperature: roughly speaking, in the conductivity range 1-10 S/cm,

samples 0 and 5 % achieved at T_d ≈1150K, are converted to nano-graphite while 20 % series in the same conductivity range retains UNCD structure. This is important to consider as conductive UNCD are preferred over nano-graphite due to superior mechanical properties, e.g., for MEMS and NEMS systems; another example include electron emitters when only diamond grains/graphitic GB provide for work function engineering through hydrogen surface termination and therefore for improved electron emissivity.

APPENDIX

LIST OF TALKS AND PAPERS

(i) "Nanodiamond to Nanographite Conversion During Field Emission", Poster Presentation, Annual Graduate Symposium, Michigan Institute for Plasma Science and Engineering (MIPSE), 2018.

(ii) "Nitrogen Doping and Graphitization Effects on Conductivity of Ultra-nanocrystalline Diamond", Poster Presentation, Engineering Graduate Research Symposium, Michigan State University, 2019.

(iii) "Nanodiamond to Nanographite Conversion During Field Emission", Talk, International Vacuum Nanoelectronics Conference (IVNC), Cincinnati, 2019.

(iv) "Field Electron Emission Induced Glow Discharge in Nanodiamond Vacuum Diode", Publication, Journal of Physics D: Applied Physics, 2019.

BIBLIOGRAPHY

BIBLIOGRAPHY

[1] Jes Asmussen and D K Reinhard. *Diamond Films Handbook*. 2010. ISBN 0824795776. doi: 10.1201/9780203910603.

[2] Y. Tzeng, M. Yoshikawa, M. Murakawa, and A. Feldman, editors. *Applications of diamond films and related materials; Proceedings of the 1st International Conference, Auburn, AL, Aug. 17-22, 1991*, volume 73, 1991.

[3] Orlando Auciello and Anirudha V. Sumant. Status review of the science and technology of ultrananocrystalline diamond (uncd™) films and application to multifunctional devices. *Diamond and Related Materials*, 19(7):699 – 718, 2010. ISSN 0925-9635. doi: https://doi.org/10.1016/j.diamond.2010.03.015. URL http://www.sciencedirect.com/science/article/pii/S092596351000141X. Proceedings of Diamond 2009, The 20th European Conference on Diamond, Diamond-Like Materials, Carbon Nanotubes and Nitrides, Part 2.

[4] X. Xiao, J. Birrell, J. E. Gerbi, O. Auciello, and J. A. Carlisle. Low temperature growth of ultrananocrystalline diamond. *Journal of Applied Physics*, 96(4):2232–2239, 2004. doi: 10.1063/1.1769609. URL https://doi.org/10.1063/1.1769609.

[5] A.R. Krauss, O. Auciello, D.M. Gruen, A. Jayatissa, A. Sumant, J. Tucek, D.C. Mancini, N. Moldovan, A. Erdemir, D. Ersoy, M.N. Gardos, H.G. Busmann, E.M. Meyer, and M.Q. Ding. Ultrananocrystalline diamond thin films for mems and moving mechanical assembly devices. *Diamond and Related Materials*, 10(11):1952 – 1961, 2001. ISSN 0925-9635. doi: https://doi.org/10.1016/S0925-9635(01)00385-5. URL http://www.sciencedirect.com/science/article/pii/S0925963501003855.

[6] Orlando Auciello, James Birrell, John A Carlisle, Jennifer E Gerbi, Xingcheng Xiao, Bei Peng, and Horacio D Espinosa. Materials science and fabrication processes for a new MEMS technology based on ultrananocrystalline diamond thin films. *Journal of Physics: Condensed Matter*, 16(16):R539–R552, apr 2004. doi: 10.1088/0953-8984/16/16/r02. URL https://doi.org/10.1088%2F0953-8984%2F16%2F16%2Fr02.

[7] A. Denisenko and E. Kohn. Diamond power devices. concepts and limits. *Diamond and Related Materials*, 14(3):491 – 498, 2005. ISSN 0925-9635. doi: https://doi.org/10.1016/j.diamond.2004.12.043. URL http://www.sciencedirect.com/science/article/pii/S0925963505000087. Proceedings of Diamond 2004, the 15th European Conference on Diamond, Diamond-Like Materials, Carbon Nanotubes, Nitrides and Silicon Carbide.

[8] M. Kasu, K. Ueda, Y. Yamauchi, A. Tallaire, and T. Makimoto. Diamond-based rf power transistors: Fundamentals and applications. *Diamond and Related Materials*, 16(4):1010 – 1015, 2007. ISSN 0925-9635. doi: https://doi.org/10.1016/j.diamond.2006.12.046. URL

http://www.sciencedirect.com/science/article/pii/S0925963506005309. Proceedings of Diamond 2006, the 17th European Conference on Diamond, Diamond-Like Materials, Carbon Nanotubes, Nitrides and Silicon Carbide.

[9] Toshiharu Makino, Norio Tokuda, Hiromitsu Kato, Masahiko Ogura, Hideyuki Watanabe, Sung-Gi Ri, Satoshi Yamasaki, and Hideyo Okushi. High-efficiency excitonic emission with deep-ultraviolet light from (001)-oriented diamondp-i-nJunction. *Japanese Journal of Applied Physics*, 45(No. 39):L1042–L1044, sep 2006. doi: 10.1143/jjap.45.l1042. URL https://doi.org/10.1143%2Fjjap.45.l1042.

[10] A. Hokazono, T. Ishikura, K. Nakamura, S. Yamashita, and H. Kawarada. Enhancement/depletion mesfets of diamond and their logic circuits. *Diamond and Related Materials*, 6(2):339 – 343, 1997. ISSN 0925-9635. doi: https://doi.org/10.1016/S0925-9635(96)00726-1. URL http://www.sciencedirect.com/science/article/pii/S0925963596007261.

[11] A. Aleksov, A. Denisenko, U. Spitzberg, T. Jenkins, W. Ebert, and E. Kohn. Rf performance of surface channel diamond fets with sub-micron gate length. *Diamond and Related Materials*, 11(3):382 – 386, 2002. ISSN 0925-9635. doi: https://doi.org/10.1016/S0925-9635(01)00644-6. URL http://www.sciencedirect.com/science/article/pii/S0925963501006446. 12th European Conference on Diamond, Diamond- Like Materials, Carbon Nanotubes, Nitrides and Silicon Carbide.

[12] Jan Isberg, Gabriel Ferro, and Paul Siffert. Diamond electronic devices. *AIP Conference Proceedings*, 1292, 11 2010. doi: 10.1063/1.3518277.

[13] M. I. Landstrass and K. V. Ravi. Resistivity of chemical vapor deposited diamond films. *Applied Physics Letters*, 55(10):975–977, 1989. doi: 10.1063/1.101694. URL https://doi.org/10.1063/1.101694.

[14] Johan F. Prins. n-type semiconducting diamond by means of oxygen-ion implantation. *Phys. Rev. B*, 61:7191–7194, Mar 2000. doi: 10.1103/PhysRevB.61.7191. URL https://link.aps.org/doi/10.1103/PhysRevB.61.7191.

[15] Isao Sakaguchi, Mikka N.-Gamo, Yuko Kikuchi, Eiji Yasu, Hajime Haneda, Toshimitsu Suzuki, and Toshihiro Ando. Sulfur: A donor dopant for n-type diamond semiconductors. *Phys. Rev. B*, 60:R2139–R2141, Jul 1999. doi: 10.1103/PhysRevB.60.R2139. URL https://link.aps.org/doi/10.1103/PhysRevB.60.R2139.

[16] S. A. Grot, C. W. Hatfield, G. Sh. Gildenblat, A. R. Badzian, and T. Badzian. Electrical properties of selectively grown homoepitaxial diamond films. *Applied Physics Letters*, 58(14): 1542–1544, 1991. doi: 10.1063/1.105172. URL https://doi.org/10.1063/1.105172.

[17] Oliver A. Williams, Michael D. Whitfield, Richard B. Jackman, John S. Foord, James E. Butler, and Christoph E. Nebel. Formation of shallow acceptor states in the surface region of thin film diamond. *Applied Physics Letters*, 78(22):3460–3462, 2001. doi: 10.1063/1.1345806. URL https://doi.org/10.1063/1.1345806.

[18] Satoshi Koizumi, Tokuyuki Teraji, and Hisao Kanda. Phosphorus-doped chemical vapor deposition of diamond. *Diamond and Related Materials*, 9(3):935 – 940, 2000. ISSN 0925-9635. doi: https://doi.org/10.1016/S0925-9635(00)00217-X. URL http://www.sciencedirect.com/science/article/pii/S092596350000217X.

[19] Hiromitsu Kato, Satoshi Yamasaki, and Hideyo Okushi. n-type doping of (001)-oriented single-crystalline diamond by phosphorus. *Applied Physics Letters*, 86(22):222111, 2005. doi: 10.1063/1.1944228. URL https://doi.org/10.1063/1.1944228.

[20] Shinichi Shikata. Single crystal diamond wafers for high power electronics. *Diamond and Related Materials*, 65:168 – 175, 2016. ISSN 0925-9635. doi: https://doi.org/10.1016/j.diamond.2016.03.013. URL http://www.sciencedirect.com/science/article/pii/S0925963516300759. Special Issue "26th International Conference on Diamond and Carbon Materials – DCM 2015".

[21] J. W. Liu, M. Y. Liao, M. Imura, E. Watanabe, H. Oosato, and Y. Koide. Diamond logic inverter with enhancement-mode metal-insulator-semiconductor field effect transistor. *Applied Physics Letters*, 105(8):082110, 2014. doi: 10.1063/1.4894291. URL https://doi.org/10.1063/1.4894291.

[22] Orlando Auciello, Pablo Gurman, Maria B. Guglielmotti, Daniel G. Olmedo, Alejandro Berra, and Mario J. Saravia. Biocompatible ultrananocrystalline diamond coatings for implantable medical devices. *MRS Bulletin*, 39(7):621–629, 2014. doi: 10.1557/mrs.2014.134.

[23] Orlando Auciello and Anirudha Sumant. Status review of the science and technology of ultrananocrystalline diamond (uncd (tm)) films and application to multifunctional devices. *Diamond and Related Materials*, 19:699–718, 07 2010. doi: 10.1016/j.diamond.2010.03.015.

[24] Piyush Bajaj, Demir Akin, Amit Gupta, Debby Sherman, Bing Shi, Orlando Auciello, and Rashid Bashir. Ultrananocrystalline diamond film as an optimal cell interface for biomedical applications. *Biomedical Microdevices*, 9(6):787–794, Dec 2007. ISSN 1572-8781. doi: 10.1007/s10544-007-9090-2. URL https://doi.org/10.1007/s10544-007-9090-2.

[25] Xingcheng Mich. Xiao, Jian Wang, Chao Liu, John Arthur Carlisle, Brian Vernon Mech, Robert G. Greenberg, Dilek Soydam Guven, Ricardo Freda, Mark S. Humayun, James D. Weiland, and Orlando H. Auciello. In vitro and in vivo evaluation of ultrananocrystalline diamond for coating of implantable retinal microchips. *Journal of biomedical materials research. Part B, Applied biomaterials*, 77 2:273–81, 2006.

[26] Alan R. Krauss, Dieter M. Gruen, Daniel Zhou, Thomas G. Mccauley, Lu Chang Qin, Timothy Corrigan, Orlando Auciello, and R. P. H. Chang. Morphology and electron emission properties of nanocrystalline cvd diamond thin films. *MRS Proceedings*, 495:299, 1997. doi: 10.1557/PROC-495-299.

[27] Dieter M. Gruen. Nanocrystalline diamond films. *Annual Review of Materials Science*, 29(1):211–259, 1999. doi: 10.1146/annurev.matsci.29.1.211. URL https://doi.org/10.1146/annurev.matsci.29.1.211.

[28] P. Keblinski, D. Wolf, F. Cleri, S.R. Phillpot, and H. Gleiter. On the nature of grain boundaries in nanocrystalline diamond. *MRS Bulletin*, 23(9):36–41, 1998. doi: 10.1557/S0883769400029353.

[29] F Cleri, P Keblinski, L Colombo, D Wolf, and S. R Phillpot. On the electrical activity ofsp2-bonded grain boundaries in nanocrystalline diamond. *Europhysics Letters (EPL)*, 46(5): 671–677, jun 1999. doi: 10.1209/epl/i1999-00318-5. URL https://doi.org/10.1209.

[30] Peter Zapol, Michael Sternberg, Larry A. Curtiss, Thomas Frauenheim, and Dieter M. Gruen. Tight-binding molecular-dynamics simulation of impurities in ultrananocrystalline diamond grain boundaries. *Phys. Rev. B*, 65:045403, Dec 2001. doi: 10.1103/PhysRevB.65.045403. URL https://link.aps.org/doi/10.1103/PhysRevB.65.045403.

[31] James Birrell, J. A. Carlisle, O. Auciello, D. M. Gruen, and J. M. Gibson. Morphology and electronic structure in nitrogen-doped ultrananocrystalline diamond. *Applied Physics Letters*, 81(12):2235–2237, sep 2002. ISSN 00036951. doi: 10.1063/1.1503153.

[32] S. Bhattacharyya, O. Auciello, J. Birrell, J. A. Carlisle, L. A. Curtiss, A. N. Goyette, D. M. Gruen, A. R. Krauss, J. Schlueter, A. Sumant, and P. Zapol. Synthesis and characterization of highly-conducting nitrogen-doped ultrananocrystalline diamond films. *Applied Physics Letters*, 79(10):1441–1443, sep 2001. ISSN 00036951. doi: 10.1063/1.1400761.

[33] Dieter M. Gruen, Xianzheng Pan, Alan R. Krauss, Shengzhong Liu, Jianshu Luo, and Christopher M. Foster. Deposition and characterization of nanocrystalline diamond films. *Journal of Vacuum Science & Technology A*, 12(4):1491–1495, 1994. doi: 10.1116/1.579343. URL https://doi.org/10.1116/1.579343.

[34] Hak-Joo Lee, Hyeongtag Jeon, and Wook-Seong Lee. Ultrananocrystalline diamond film deposition by direct-current plasma assisted chemical vapor deposition using hydrogen-rich precursor gas in the absence of the positive column. *Journal of Applied Physics*, 109(2): 023303, 2011. doi: 10.1063/1.3533764. URL https://doi.org/10.1063/1.3533764.

[35] Sobia Allah Rakha, Guojun Yu, Jianqing Cao, Suixia He, and Xingtai Zhou. Influence of ch4 on the morphology of nanocrystalline diamond films deposited by ar rich microwave plasma. *Journal of Applied Physics*, 107(11):114324, 2010. doi: 10.1063/1.3410804. URL https://doi.org/10.1063/1.3410804.

[36] Dieter M. Gruen. Ultrananocrystalline diamond in the laboratory and the cosmos. *MRS Bulletin*, 26(10):771–776, 2001. doi: 10.1557/mrs2001.204.

[37] P. Achatz, O. A. Williams, P. Bruno, D. M. Gruen, J. A. Garrido, and M. Stutzmann. Effect of nitrogen on the electronic properties of ultrananocrystalline diamond thin films grown on quartz and diamond substrates. *Physical Review B - Condensed Matter and Materials Physics*, 74(15), 2006. ISSN 10980121. doi: 10.1103/PhysRevB.74.155429.

[38] Oliver A. Williams, Stephane Curat, Jennifer E. Gerbi, Dieter M. Gruen, and Richard B. Jackman. n-type conductivity in ultrananocrystalline diamond films. *Applied Physics Letters*, 85(10):1680–1682, 2004. doi: 10.1063/1.1785288. URL https://doi.org/10.1063/1.1785288.

[39] James Birrell, J. E. Gerbi, O. Auciello, J. M. Gibson, D. M. Gruen, and J. A. Carlisle. Bonding structure in nitrogen doped ultrananocrystalline diamond. *Journal of Applied Physics*, 93(9): 5606–5612, 2003. ISSN 0021-8979. doi: 10.1063/1.1564880.

[40] Tomohiro Ikeda, Kungen Teii, C. Casiraghi, J. Robertson, and A. C. Ferrari. Effect of the s p2 carbon phase on n -type conduction in nanodiamond films. *Journal of Applied Physics*, 104 (7), 2008. ISSN 00218979. doi: 10.1063/1.2990061.

[41] J.J. Alcantar-Peña, J. Montes, M.J. Arellano-Jimenez, J.E. Ortega Aguilar, D. Berman-Mendoza, R. García, M.J. Yacaman, and O. Auciello. Low temperature hot filament chemical vapor deposition of ultrananocrystalline diamond films with tunable sheet resistance for electronic power devices. *Diamond and Related Materials*, 69:207 – 213, 2016. ISSN 0925-9635. doi: https://doi.org/10.1016/j.diamond.2016.09.007. URL http://www.sciencedirect.com/science/article/pii/S0925963516303284.

[42] James E. Butler and Anirudha V. Sumant. The cvd of nanodiamond materials. *Chemical Vapor Deposition*, 14(7-8):145–160, 2008. doi: 10.1002/cvde.200700037. URL https://onlinelibrary.wiley.com/doi/abs/10.1002/cvde.200700037.

[43] Neda Wiora, Michael Mertens, Kai Brühne, H.-J Fecht, Ich C. Tran, Trevor Willey, Anthony van Buuren, Juergen Biener, and Jun-Sik Lee. Grain boundary dominated electrical conductivity in ultrananocrystalline diamond. *Journal of Applied Physics*, 122:145102, 10 2017. doi: 10.1063/1.4993442.

[44] James Birrell, J.E. Gerbi, O. Auciello, J.M. Gibson, J. Johnson, and J.A. Carlisle. Interpretation of the raman spectra of ultrananocrystalline diamond. *Diamond and Related Materials*, 14(1):86 – 92, 2005. ISSN 0925-9635. doi: https://doi.org/10.1016/j.diamond.2004.07.012. URL http://www.sciencedirect.com/science/article/pii/S0925963504002596.

[45] James E. Butler and Richard L. Woodin. *Thin film diamond growth mechanisms*, pages 15–30. Springer Netherlands, Dordrecht, 1994. ISBN 978-94-011-0725-9.

[46] H. R. Phillip and E. A. Taft. Kramers-kronig analysis of reflectance data for diamond. *Phys. Rev.*, 136:A1445–A1448, Nov 1964. doi: 10.1103/PhysRev.136.A1445. URL https://link.aps.org/doi/10.1103/PhysRev.136.A1445.

[47] M. A. Pimenta, G. Dresselhaus, M. S. Dresselhaus, L. G. Cançado, A. Jorio, and R. Saito. Studying disorder in graphite-based systems by Raman spectroscopy. *Physical Chemistry Chemical Physics*, 9(11):1276–1291, 2007. ISSN 14639076. doi: 10.1039/b613962k.

[48] A. C. Ferrari and J. Robertson. Interpretation of raman spectra of disordered and amorphous carbon. *Phys. Rev. B*, 61:14095–14107, May 2000. doi: 10.1103/PhysRevB.61.14095. URL https://link.aps.org/doi/10.1103/PhysRevB.61.14095.

[49] O. Gröning, O. M. Küttel, P. Gröning, and L. Schlapbach. Field emission properties of nanocrystalline chemically vapor deposited-diamond films. *Journal of Vacuum*

Science & Technology B: Microelectronics and Nanometer Structures Processing, Measurement, and Phenomena, 17(5):1970–1986, 1999. doi: 10.1116/1.590857. URL https://avs.scitation.org/doi/abs/10.1116/1.590857.

[50] R. Pfeiffer, H. Kuzmany, N. Salk, and B. Günther. Evidence for trans-polyacetylene in nanocrystalline diamond films from h–d isotropic substitution experiments. *Applied Physics Letters*, 82(23):4149–4150, 2003. doi: 10.1063/1.1582352. URL https://doi.org/10.1063/1.1582352.

[51] Stanislav Baturin, Tanvi Nikhar, and Sergey Baryshev. Field electron emission induced glow discharge in nanodiamond vacuum diode. *Journal of Physics D: Applied Physics*, 2019. URL http://iopscience.iop.org/10.1088/1361-6463/ab2183.